# INVESTIGATION OF CRYPTOTEPHRA

# IN POLAR ICE CORES

By

Meredith Helmick

B.S. Concord University, 2020

A THESIS

Submitted in Partial Fulfillment of the

Requirements for the Degree of

Master of Science

(in Earth and Climate Science)

The Graduate School

The University of Maine

December 2022

Advisory Committee:

Dr. Andrei Kurbatov, Associate Professor, Climate Change Institute and School of Earth and Climate Sciences, Advisor

Dr. Martin Yates, Lab Manager/Instructor, School of Earth and Climate Sciences

Dr. Nelia Dunbar, Director, New Mexico Bureau of Geology and Mineral Resources

Dr. Katherine Glover, Research Associate, Climate Change Institute

© 2022 Meredith Helmick

All Rights Reserved

**INVESTIGTATION OF CRYPTOTEPHRA**

**IN POLAR ICE CORES**

By Meredith Helmick

Thesis Advisor: Dr. Andrei Kurbatov

An Abstract of the Thesis Presented
in Partial Fulfillment of the Requirements for the
Degree of Master of Science
(in Earth and Climate Science)
December 2022

Volcanic ash (tephra) present within polar ice cores greatly supplements our understanding of past volcanism and its impacts on society and the state of the climate system. This thesis investigates the utility and limitations of ice core tephrochronology in answering questions related to volcanic source identification of ice core glaciochemical signals, tephrostratigraphy of an Antarctic ice core, and the timing of major and climate forcing eruptions.

This thesis explores the efficacy of SEM-EDS measurements on ultra-fine (<10 μm) volcanic particles for the purpose of geochemically characterizing a non-visible ice-embedded tephra and the subsequent identification of the volcanic source. In combination with other lines of evidence, such as the timing and deposition of microparticles and volcanic sulfate to the Antarctic ice sheet at South Pole, we hypothesize that the volcanic source of a dated 1880's non-visible tephra layer in the South Pole Ice Core can be linked to the 1886 CE eruption of Tarawera, Okataina Volcanic Center, New Zealand. This study also highlights the complexities of volcanic source determinations using ultra-fine particles and SEM-EDS,

especially when possible volcanic sources are close in composition, as is the case with eruptive products of the Okataina Volcanic Center and 1883 CE Krakatau. Volcanic source aside, we present the cryptotephra layer discovered at 23.61-23.79 meters depth of the South Pole Ice Core as a potential tephrochronological maker for the correlation of paleoclimate datasets.

Geochemical data presented in Appendix B establishes the foundations for a South Pole Ice Core tephrostratigraphic record with novel cryptotephra layers discovered at ~1882 CE, ~1600 CE, ~3518 BCE, ~4526 BCE, ~8127 BCE, and ~9214 BCE (all dates are based on SP19 timescale).

Geochemical data presented in Appendix D is the University of Maine's contribution to a PNAS Nexxus publication. Our analyses of cryptotephra from the GISP2 ice core helped to determine Aniakchak II as the source of a dated 1628 BCE volcanic signal and constrain the timing of the infamous Minoan eruption of Santorini.

**DEDICATION**

This thesis is dedicated to all those who have helped me get here

in some *way, shape, form, or fashion.*

**ACKNOWLEDGEMENTS**

This work is supported by the National Science Foundation grants PLR-1543454 and 1543361. We thank the U.S. Ice Drilling Program for support activities through NSF Cooperative Agreement 1836328, SPICE Ice Core recovery, research, and logistical team and the NSF Ice Core Facility for allocation and storage of the SPC14 ice core

Thank you to the UMaine and CCI ice core crew for all your time and assistance regarding freezer work, sample preparation, and maintaining my sanity (I'm looking at you Lizi, Hanna, and Kevin). I look forward to watching your budding careers unfold in front of you and wish you all the very best. Thank you to Nels Iverson and Dominic Winski for signing on to read and critique this work. Special thanks to Jennifer Phillippe, Stephen Kuehn, and Alicia Cruz-Uribe; you have been guiding lights throughout my navigation of this experience.

Finally, the author would like to express thanks to her advisor and committee. This has been a wonderful learning experience and I am immensely grateful for this opportunity.

**TABLE OF CONTENTS**

## LIST OF TABLES

## LIST OF FIGURES

# CHAPTER 1

## INTRODUCTION

Volcanogenic sulfate and tephra particles are well-preserved in polar ice and provide a continuous record of the atmospheric loading of volcanic products. Concentrations of sulfate (Cole-Dai et al., 2000; Sigl et al., 2015; Toohey and Sigl, 2017) and/or the magnitude of electrical conductivity (ECM) in ice cores (Hammer et al., 1980; Fudge et al., 2016) are well-established metrics for reconstructing the history of past volcanism and evaluating the climate forcing of volcanic events (Robock, 2000). Nevertheless, only by the geochemical characterization or "fingerprinting" of tephra (Dunbar et al., 2017) can secure volcanic source determinations be made for glaciochemical volcanic signals in ice. Once accurate volcanic source determinations can be made the physical features of the tephra can provide a wealth of information on eruption timing, magnitude, syn-eruptive atmospheric transport mechanisms. In addition, a well-dated and/or well-characterized tephra layer may serve as an isochronous marker in the stratigraphic correlation of ice cores and other sedimentary archives.

Tephra layers found in polar ice cores, however, often exists as non-visible cryptotephras (Lowe and Hunt, 2001) composed of ultra-fine (generally < 10 μm) and sparsely concentrated particles. Small particle and typically low particle numbers contribute to the inherent difficulty of ice core tephra work, especially because availability of ice core samples is typically limited. Improvements in the methodology used to capture, extract, and measure these cryptotephras (Palais et al., 1990; Dunbar et al., 2003; Kuehn and Froese, 2010; Iverson et al., 2016; Hartman et al., 2019; Plunkett et al., 2020; Pearson et al., 2022) have greatly enhanced the accuracy and robustness of fingerprinting ice core cryptotephras.

The primary focus of this thesis is to explore the applications and limitations of ice core tephrochronology using novel and tested sample preparation and analytical methodologies. The core of the thesis is a manuscript to be submitted for peer-review which explores the use of recent methodological advancements to examine the volcanic source of a cryptotephra deposit discovered in a dated 1880's interval of the South Pole Ice Core (SPC14). This work highlights the complexity and limitations of analyzing particles < 10 µm in diameter, and how best to approach source determinations when possible volcanic sources exhibit similar compositions. Particle geochemistry of cryptotephras from additional depth intervals of the South Pole Ice Core are included in Appendix A. Geochemical data related to the University of Maine's contribution to the collaborative paper (Pearson et al., 2022) published in PNAS Nexxus can be found in Appendix D. Finally, an unabridged example of our sample preparation and analysis procedures can be found in Appendix C.

# CHAPTER 2

# TARAWERA 1886 CE VOLCANIC PRODUCTS IN ANTARCTIC ICE CORES


## Summary

The correct identification and precise dating of explosive volcanic eruptions in polar ice cores are critical for investigating volcanic influence on climate and for constraining ice core timescales. Antarctic ice core records show increased volcanic sulfate concentrations in the 1880s CE, which have been attributed to the 1883 CE eruption of Krakatau, Indonesia, and the 1886 CE eruption of Tarawera, Okataina Volcanic Center, New Zealand. In the South Pole ice core (SPC14), the onset of the first sulfate increase is dated as 1883 in the current SP19 timescale based on annual layer counting and comprehensive volcanic signals matched to the WDC-06A ice core. Here we present new scanning electron microscopy and energy dispersive spectroscopy (SEM-EDS) analyses of microscopic volcanic glass shards extracted from the SPC14 core depth (23.61-23.79m) interval that immediately precedes the onset of the increased volcanic sulfate concentrations previously attributed to the Krakatau eruption. Several lines of evidence indicate that this volcanic deposit is likely affiliated with a unique phase of the 1886 CE eruption of Tarawera, which could impact established Antarctic ice core timescales.


## Introduction

Polar ice cores preserve unrivaled pre-instrumental records of past explosive volcanism (Hammer et al., 1980; Zielinski, 1995; Sigl et al., 2015; Toohey and Sigl, 2017). These ice archives record the deposition of insoluble (tephra) and soluble particles (aerosols) (Zielinski et al., 1997; Zdanowicz et al., 1999; Zielinski, 2000) delivered from global and regional eruptions (Basile et al., 2001; Dunbar et al., 2003; Narcisi et al., 2005, 2010, 2012, 2017; Dunbar et al., 2008; Dunbar

and Kurbatov, 2011). The atmospheric loading of volcanic aerosols, estimated by measuring ice core concentrations of sulfate (Cole-Dai et al., 2000; Sigl et al., 2015; Toohey and Sigl, 2017) or the magnitude of electrical conductivity (ECM) (Hammer et al., 1980; Fudge et al., 2016), has been used to quantify climate forcing of volcanism. While it is possible to differentiate among tropospheric and stratospheric volcanic product delivery pathways (Baroni et al., 2007; Burke et al., 2019; Pearson et al., 2022) using sulfur isotopes, sulfate and ECM based data do not help with volcanic transport determinations. Sulfate and ECM signals are inherently anonymous and not diagnostic of a given eruption (Lemieux-Dudon et al., 2010), and in practice exhibit complex spatial depositional patterns (Coulter et al., 2012). Thus, limited understanding of volcanic products' atmospheric transport hinders the ability to fully evaluate the impact of a specific eruption on the climate system.

Conversely, the physical and unique geochemical properties of volcanic ash (tephra), specifically the glass composition, can be used to identify the volcanic source of past eruptions preserved in ice. Volcanic glasses tend to be compositionally distinct, and characteristic of a given volcano or specific volcanic event (Lowe et al., 2017). Therefore, the characterization of volcanic glass within ice-embedded tephra deposits can be used to accurately assign a volcanic source and timing of an event to volcanic horizons observed in ice cores (e.g., Zielinski et al., 1997; Palais et al., 1990; Kurbatov et al., 2006; Dunbar and Kurbatov, 2011).

Beyond the identification of volcanic sources, tephra has proven to be a useful tool in the correlation of geological, archaeological, and paleoenvironmental archives due to its nearly instantaneous deposition (Wallace et al., 2022). Carefully fingerprinted deposits, even when a volcanic source cannot be accurately identified, are excellent time-stratigraphic markers which

can be employed to correlate across various depositional sequences including ice cores (Dunbar et al., 2003; Narcisi et al., 2012). Further, it is possible to employ well-characterized ice-embedded tephras in the construction of ice chronologies via the identification of isochronous time markers (Coulter et al., 2012; Dunbar et al., 2017) and to validate those chronologies already existing (Dunbar et al., 2003; Vinther et al., 2006; Coulter et al., 2012).

Ideal volcanic glass fingerprinting methods employ electron microprobe equipped with wavelength dispersive spectroscopy (EMP-WDS) to precisely analyze geochemical compositions of individual glass shards. However, these methods are not always suitable for analyzing the fine-grained material (cryptotephra) from remote or tropical eruptions typically captured in Antarctic ice cores (e.g., Vostok: Palais et al., 1987; Basile et al., 2001; Dunbar, et al. 2003; Taylor Dome: Dunbar et al., 2003; Talos Dome: Narcisi et al., 2010, 2017; Moulton: Dunbar et al., 2008; Patriot Hills: Turney et al., 2020). Recent advances in methodology and instrumentation (Iverson et al., 2017; Hartman et al., 2019) have improved the ability to detect, extract, and geochemically fingerprint ice core cryptotephras. Analytical methods utilizing SEM-EDS (scanning electron microscope + energy dispersive spectroscopy) on unpolished sample mounts, despite yielding less precise geochemical measurements than EMP-WDS (Iverson et al., 2017), can be a useful alternative for characterizing the small (<10 μm) cryptotephra glass shards. When used simultaneously with stratigraphic, paleoenvironmental, and chronological criteria, SEM-EDS measurements contribute to a comprehensive framework to identify the origin of ice core cryptotephras.

An increased sulfate signal in the 1880s is well represented in sulfate profiles from various Antarctic ice cores. Several developed sulfate-based volcanic loading reconstructions

(e.g., Delmas et al., 1992; Palmer et al., 2001; Kurbatov et al., 2006; Jiang et al., 2012; Plummer et al., 2012; Sigl et al., 2013) have interpreted this anomaly as evidence of volcanic aerosol deposition from the 1883 CE eruption of Krakatau, Indonesia, and the 1886 CE eruption of Tarawera, Okataina Volcanic Center, New Zealand. In this study, we investigate the volcanic source of this sulfate anomaly by applying new methodology to capture and measure the geochemical composition of cryptotephra from the South Pole ice core (SPC14) at 23.6-23.8m depth. Our results indicate that the cryptotephra preserved in SPC14 better matches rhyolitic material from the Tarawera (1886) eruption of the Okataina Volcanic Center (OVC), New Zealand.

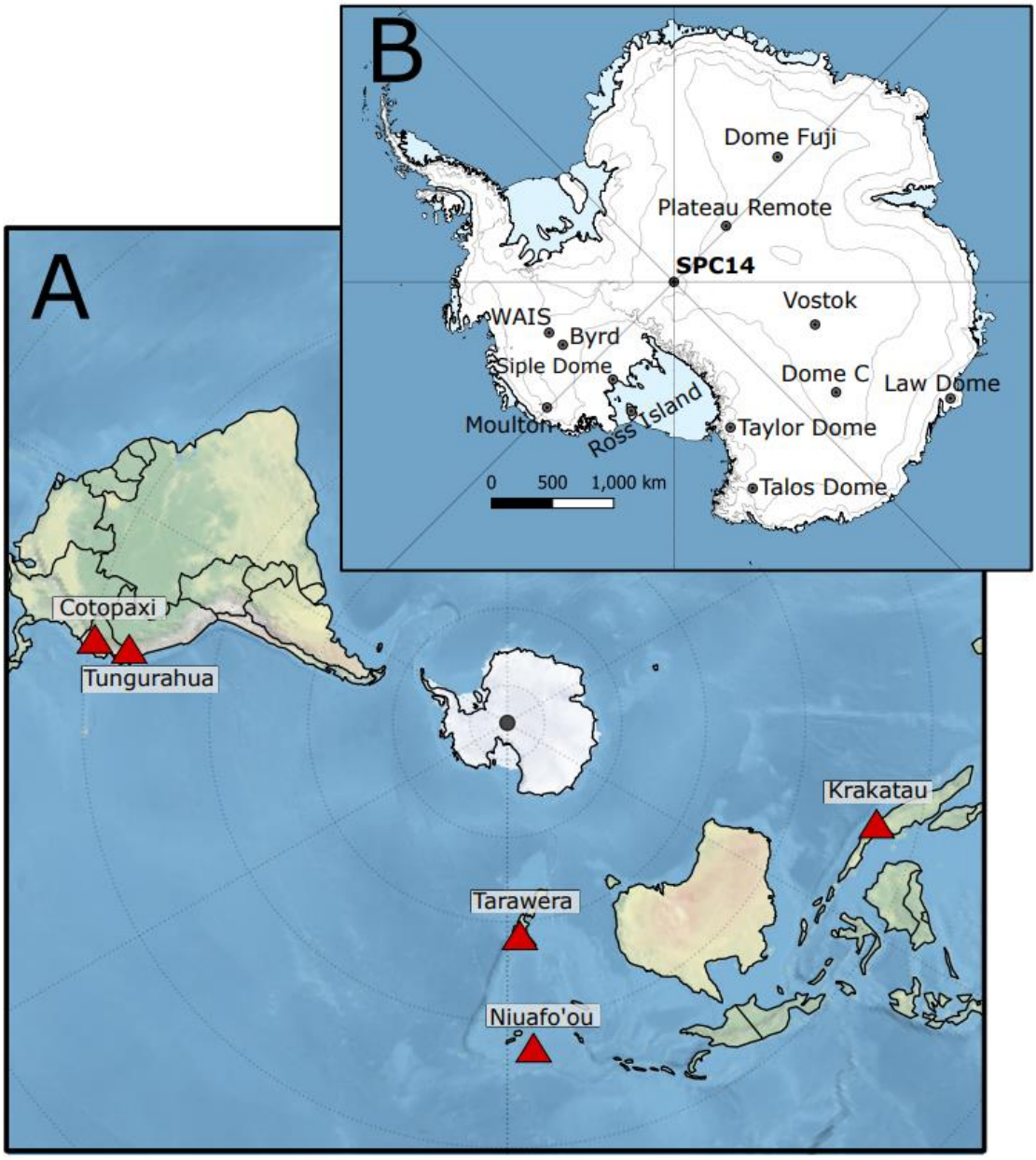


**Figure 2.1.** Map of Potential Volcanic Sources. (A) Location of evaluated potential volcanic sources discussed in this paper (red triangles) and (B) Antarctic ice cores including the SPC14 site. Created with Cartopy v 0.18.0 and Python 3.9.7 and Quantarctica 32 (Matsuoka et al., 2021).

**Methods**

The South Pole Ice Core (SPC14) was drilled at 89.99° S, 98.16° W (Fig. 1) to a final depth of 1751m over the 2014-2016 austral summers (Souney et al., 2021) and captures a continuous 54,000-year (Winski et al., 2019) paleoclimate record. SPC-14 provides the first environmental and climate record of the past 40 ka from the South Pole sector of East Antarctica (Casey et al., 2014), extending the spatial array of 40 ka+ Antarctic ice cores to 82° S. The average accumulation rate (7.4 cm w.e. a-1) (Winski et al., 2019) permits sub-annual glaciochemical measurements utilized for annual layer counting to 11,300 years BP. The SP19 timescale complemented annual layer counting by volcanic signal synchronization with the WDC-06A ice core from West Antarctica.

To determine the volcanic source of the 1880s volcanic interval, we sampled the SPC14 22.90-24.20 depth interval to resolve the source of cryptotephra associated with the complex sulfate (Winski, 2021), conductance (Lilien et al., 2018) and microparticles concentration anomalies (Fig. 2). All tephra sampling was conducted in an ultra-clean cold laboratory at the University of Maine. Each frozen sample was cut using a pre-cleaned coping saw and decontaminated by shaving off the outermost ~1mm. Decontaminated samples were transferred to 0.7L Whirl-Pak® bags and transported frozen to an ambient clean room laboratory. There, each sample was rapidly melted by placing the sealed Whirl-Pak® into a ~40°C warm water bath. The sample meltwater was immediately transferred into clean 15 ml vials and centrifuged at 5000 RPM for 10 minutes. Forty microliters of sample meltwater were then pipetted from the bottom of each vial onto the center of a plastic Buehler mounting ring adhered to a 4x4 cm square of single-sided 4-mil Kapton tape. The entire mount (mounting ring

+ tape) was affixed to an ultra-flat 1mm thick metal surface preheated to 65°C on a hot plate. After the meltwater completely evaporated, the mount was back-filled with Buehler Epo-Thin 2 epoxy. The epoxy resin was carefully mixed, preheated to ~40°C and degassed in a vacuum chamber for 5 minutes before application to avoid bubbles.

Each mount was fully cured (12 hours) before ultrasound cleaning in distilled water for five minutes. Trapped on the surface of each mount, particles were coated with a 15 nm layer of carbon using an Emitech high vacuum evaporator and analyzed using the University of Maine's Tescan Vega II XMU tungsten filament scanning electron microscope (SEM) equipped with an EDAX Apollo SSD40 energy dispersive spectrometer (EDS). Unpolished particles were identified via backscatter (BSE) and secondary electron (SE) imaging modes and subsequently analyzed on a single spot with a 120-pA focused beam for 100 seconds of live time at 15kV accelerating voltage. Ten major element oxides were calculated and adjusted using the semi-quantitative EDAX Genesis PhiRhoZ internal quantification procedure and the USNM 72854 VG-568 rhyolitic glass standard. Analytical accuracy was tested by analyzing additional reference materials during each operating session.

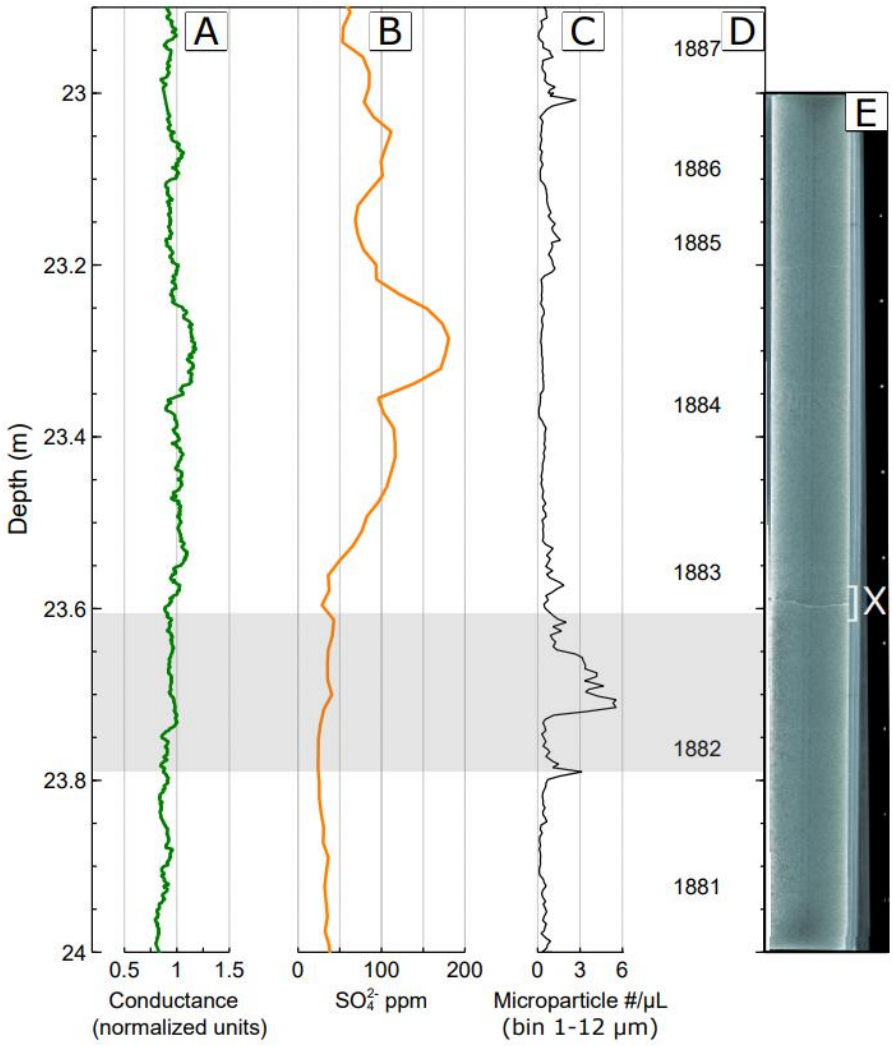


**Figure 2.2**. Depth Profile of Targeted SPC14 Interval. SPC14 conductance (A), sulfate concentration (B), and microparticle concentration (C) variation with depth and interpolated age in calendar year (D). Volcanic glass shards described in this study were extracted from the 23.61-23.79 m depth interval, highlighted in gray. An optical scan image acquired during ice core processing at the U.S. NSF Ice Core Facility (right) by Geoffrey Hargreaves shows no visible tephra at these depths; a break in the core (X) is visible at ~ 23.60m. In subsampling, the 23.61-23.79m section began at this break. This observed offset is likely related to depth error due to ice handling, processing, and cleaning.

Of eight (5-23 cm long) sampling sections (Appendix A.1), only the 23.61-23.79m depth section was found to contain a significant (>100) number of particles. Unpolished particles were first analyzed under the aforementioned SEM-EDS operating conditions. To reduce X-ray geometric effects and increase analytical accuracy (Goldstein et al., 2018), the sample was hand-polished using 0.50 and 0.25 µm polishing paste, carbon coated, and reanalyzed during two additional SEM-EDS sessions (sessions 2 and 3). Session 2 was performed on the polished mount under identical SEM-EDS operating conditions as session 1 (unpolished mount), and session 3 was performed with an increased collection time of 200 live seconds on the polished mount, all else equivalent (Appendix A.2.). Due to minor particle loss and alteration, it is difficult to obtain repeat analyses on the same particles; therefore, particles analyzed across the three sessions were selected randomly and may not have been the same particles.

**Results**

Hundreds of ultra-fine particles were only observed in the 23.61-23.79m depth interval of SPC14. Particle radii ranged from 1 µm to 10 µm (longest axis measurement). A total of 20 analyses were performed on the largest particles across three analytical sessions.

The volcanic glass shards' composition, measured using SEM-EDS, is rhyolitic with ~77 wt.% $SiO_2$, ~12 wt.% $Al_2O_3$, and ~3 wt.% $Na_2O$ and $K_2O$ (Fig. 3 and Appendix A.3.). These values represent the averages across all three analytical sessions. Measured values of MgO, $P_2O_5$, CaO, $TiO_2$, and MnO are near or less than ~1 wt.% effectively below method detection limit (Iverson et al., 2017). Measured abundances of the most robust major element oxides range from approximately 75 to 80 wt.% $SiO_2$; 10 to 14 wt.% $Al_2O_3$; 2 to 5 wt.% $K_2O$; 1 to 5 wt.% $Na_2O$; 1 - 3 wt.% FeO; and below 2 wt. % CaO across all sessions. A 2% uncertainty for SEM-EDS

analyses was reported in Iverson et al. (2017) and we observed similar values on the secondary reference materials (Appendix A.4.).

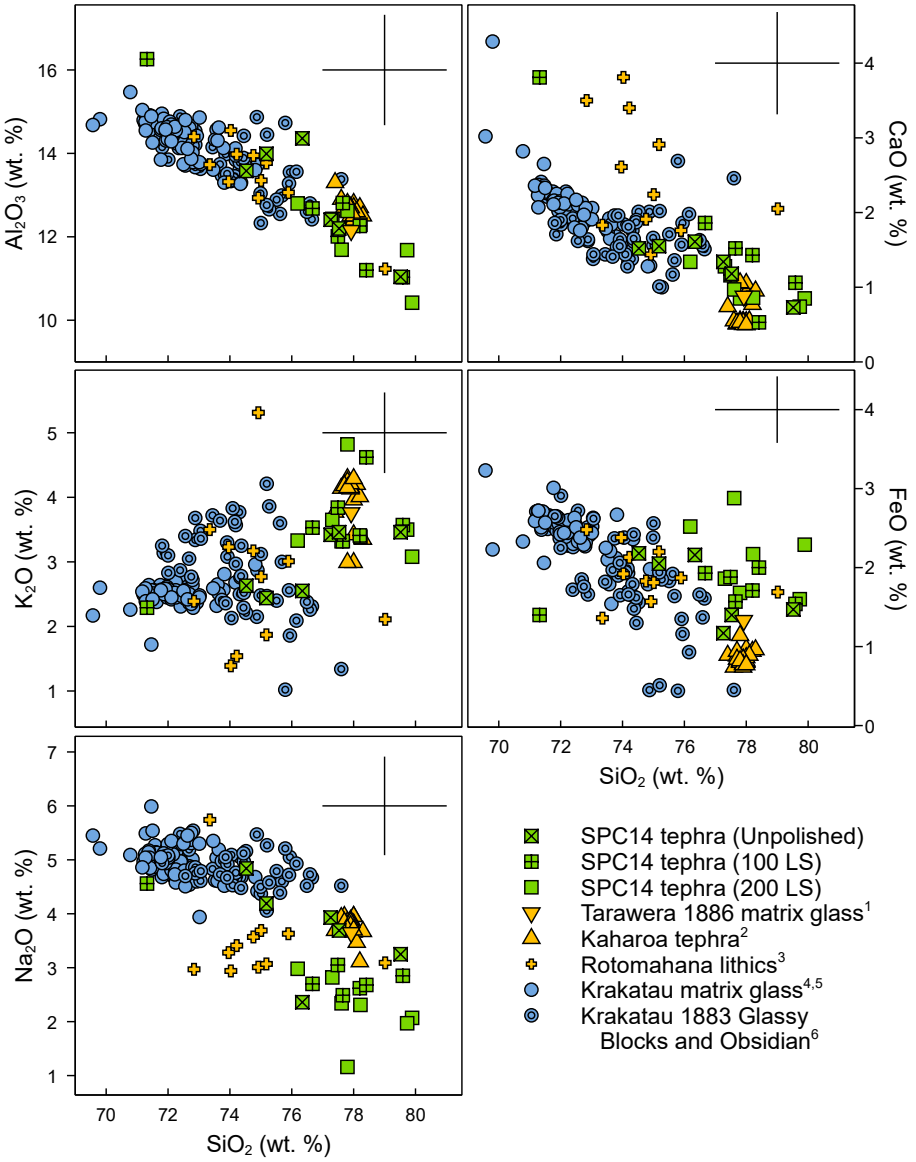


**Figure 2.3.** Harker Diagrams (23.61-23.79m). Geochemical composition of individual volcanic glass shards extracted from the 23.61-23.79m section of the SPC14 ice core compared with possible volcanic sources from the Okataina Volcanic Center ([1] Hughes et al., 2021; [2] Hopkins et al., 2021; [3] Pittari et al., 2016) and Krakatau ([4] Mandeville et al., 1996; [5] Madden-Nadeau et al., 2021; [6] Madden-Nadeau, 2020) via bivariate diagrams.

We observed some variation between the three SEM-EDS analytical sessions. Notably, we observe a decrease in average measured $Na_2O$ in the second and third sessions, when compared with the first analytical session. The variation in measurements can likely be attributed to a combination of geometric effects due to sample topography between the unpolished and polished grains, small particle size, and the migration of Na during the extended counting time of the third analytical session.

**Discussion**

Geochemical data collected by SEM-EDS on small <10 μm particles will have large analytical errors (see for details, Iverson et al., 2017). However, when geochemical fingerprinting data used in conjunction with stratigraphic, paleoenvironmental, and chronological criteria, the low-precision EDS data can be useful in tephra correlations; especially when they provide a means to discount compositionally distinct (e.g., rhyolite vs. trachyte) volcanic sources. Our search for a source volcano was limited to a relatively narrow range of possible source eruptions around 1880 CE. We initially selected five southern hemisphere eruptions (Fig. 1) of sizable magnitude known to have occurred within a ten-year time window centered at 1882 CE (1877-1887) as possible volcanic sources of the SPC14 cryptotephra: Cotopaxi, Ecuador (1877); Krakatau, Indonesia (1883); Tungurahua, Ecuador (1886); Okataina (Tarawera), New Zealand (1886), and Niuafo'ou, Tonga (1886) (Global Volcanism Program, 2013). Published compositions for Cotopaxi (Saalfeld, 2018), Tungurahua (Hall et al., 1999), and Niuafo'ou (Taylor, 1991) volcanic products are distinct from the rhyolitic SPC14 tephra composition; thereby discounting each as potential sources, leaving only the suspected 1883 CE. eruption of Krakatau, Indonesia and the

1886 CE eruption of Tarawera, Okataina Volcanic Center (OVC), New Zealand, as the possible candidates.

The geochemical fingerprint of the SPC14 cryptotephra is similar to that of both the most evolved products of the Krakatau eruption (Madden-Nadeau, 2020; Madden-Nadeau et al., 2021), and recently reported rhyolitic products (Hughes et al., 2021) associated with the Tarawera (1886) eruption. Pyroclastic products of the 1883 CE eruption of Krakatau have been the subject of many investigations (Stehn, 1929; Westerveld, 1952; Self and Rampino, 1981; Self, 1992; Mandeville et al., 1996) and are predominantly andesites and dacites, with lesser occurrences of high-alumina basalts and rhyolites. Recently exposed stratigraphic sections of 1883 eruptive deposits have revealed units with previously unknown evolved compositions ($SiO_2$ concentrations as high 77.6 (wt.%), Madden-Nadeau, 2020; Madden-Nadeau et al., 2021). We find that of the most evolved Krakatau products, the geochemical signature of the SPC14 cryptotephra is most similar to matrix glasses (Madden-Nadeau, 2020) and glassy lava blocks and obsidians from the sub-plinian (May) and paroxysmal (August) phases of the 1883 CE eruption (see Fig. 3, refs., 5 and 6).

It is important to note that rhyolitic pyroclastic products of the 1886 CE eruption of Tarawera (1886) and pre-1886 rhyolites of the Okataina Volcanic Center also share affinities with the geochemical signature of the SPC14 cryptotephra. Despite the notoriety of the Tarawera (1886) fissure event as being one of the few documented basaltic plinian eruptions (Cole et al., 1970; Walker et al., 1984), the greater OVC is characterized by high-silica rhyolitic eruptions and is among the most productive rhyolite centers on the planet (Wilson et al., 1995). Prior to the Tarawera (1886) event, the ~1314 CE Kaharoa event, the largest New Zealand

eruption of the past 1000 years (Leonard et al., 2002), was the most recent eruption from Mt. Tarawera and the OVC. The incorporation of rhyolitic components in Tarawera (1886) deposits has been thoroughly documented (Nairn, 1979; Walker et al., 1984; Carey et al., 2007; Rosseel et al., 2006; Pittari et al., 2016). These occurrences have generally been interpreted as remnants of pulverized and non-juvenile Kaharoa pumice deposits (Walker, 1984) and pre-1886 wall rock of the OVC (Sable et al., 2009; Pittari et al., 2016) mobilized by the explosive stages of the eruption, and interaction of the rising basaltic magma with cold Kaharoa rhyolites (Hughes et al., 2021). Of the known rhyolitic Tarawera (1886) products, we find rhyolitic lithic clasts from the Rotomahana pyroclastic deposits (Pittari et al., 2016), Kaharoa rhyolites (Hopkins et al., 2021), and a rhyolitic Tarawera (1886) matrix glass (Hughes et al., 2021) to be the most similar to the geochemical signature of the SPC14 cryptotephra (see Fig. 3 refs., 3, 2, and 1).

As previously mentioned, the low-precision geochemical measurements of small particles via SEM-EDS prevent multi-element geochemical fingerprinting with the potential source tephras. To resolve the source of SPC14 cryptotephra and select from most evolved volcanic products of the 1883 CE eruption of Krakatau, or the rhyolitic fraction of the 1886 CE eruption of Tarawera, we consider additional parameters in our stratigraphic correlation.

According to a recent volcanic cloud dispersal modeling study by Stenchikov et al. (2021), the atmospheric residency times of fine (0.1-10 μm) volcanic ash particles vary distinctly by particle radius (r). Model results indicate that in a Pinatubo-sized eruption cloud injected into the tropical tropopause (17km), ash particles with radii 6 - 10 μm settled almost completely within two weeks of injection (Stenchikov et al., 2021). Finer particles 3 - 6 μm were deposited within the first month, and the finest particles $r < 1.8$ μm remained aloft for several

months post injection. Due to our identification of volcanic glass shards as large as 10 µm within the SPC14 cryptotephra (Fig. 4), we deduce that the volcanic material was rapidly transported through the troposphere to Antarctica in a period of less than two weeks from the source volcano. Similar rapid tropospheric transport of volcanic material to Antarctica has been documented via satellite imagery for the 2011 eruption of Puyehue-Cordón Caulle, Chile (Koffman et al., 2017), and modeled for the Oruanui (~26500 BCE) eruption of Taupo volcano, New Zealand (Dunbar et al., 2017).

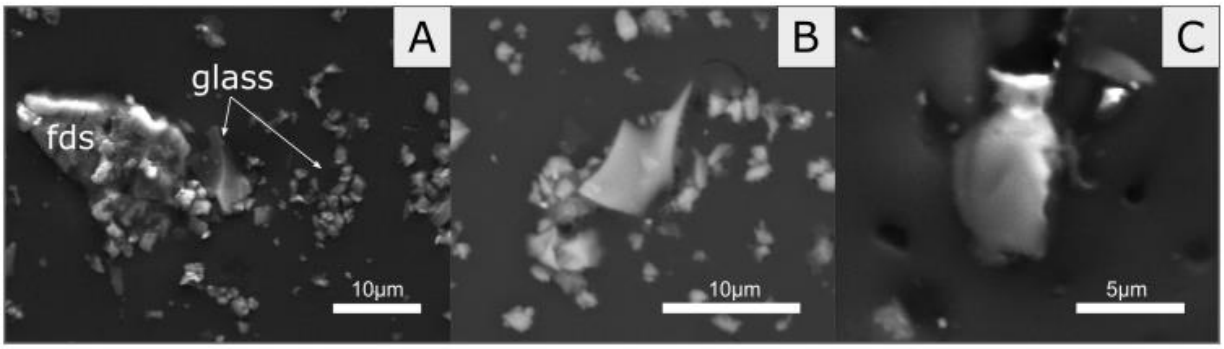


**Figure 2.4.** Selected Cryptotephra Particle Images. Images captured from the 23.61-23.79m SPC14 depth section, with the largest particles displaying typical volcanic glass morphologies. Panels 4A and 4B illustrate the amount of fine volcanic particles present in this section.

According to the current tephra framework of Antarctica (Basile et al., 2001; Dunbar et al., 2003; 2017; Narcisi et al., 2010; 2017; Hartman et al., 2019), typical long range regional sources include Antarctic, sub-Antarctic, South American, and New Zealand volcanic centers. Owing to the 1886 CE eruption of Tarawera being the only known eruption with a rhyolitic pyroclastic component from a non-tropical regional volcanic source during the 1877-1887 CE period, we posit that Tarawera is likely the source of the SPC14 cryptotephra. We understand

that the correlation of a rhyolitic cryptotephra to a basaltic-plinian eruption may be concerning.

The Tarawera fissure erupted through rhyolitic domes constructed by previous volcanic activity of the OVC (Cole, 1970), and prompted phreatomagmatic explosions which excavated fine lake sediments from Lake Rotomahana (Nairn, 1979; Keam, 2016) and pulverized rhyolitic wall rock. Additionally silicic melt inclusions (Rowe et al., 2021) and rhyolitic matrix glass (Hughes et al., 2021) identified amongst the Tarawera deposits are suggestive of an interaction between the rising basaltic magma and the rhyolitic wall rock along the fissure. It is plausible that fine-grained rhyolitic lake sediments, wall rock fragments, or glass shards from a small and unknown silicic eruption stage generated by the interaction of rhyolitic material with the basaltic melt were entrained in the volcanic plume over Tarawera and rapidly transported to the South Pole under favorable rapid atmospheric transport conditions.

The possible identification of Tarawera volcanic products in the SPC14 ice core raises implications regarding the tephrostratigraphy and volcanic hazards of New Zealand, and Antarctic ice core timescales.

Our findings highlight the potential threat long range transport of fine ash may pose to regional aviation safety (see Prata and Rose, 2015; Casadevall, 1994). Therefore, we stress that the possible long-range transport of fine volcanic ash, such as from Tarawera to Antarctica, be carefully documented for future volcanic hazard assessments.

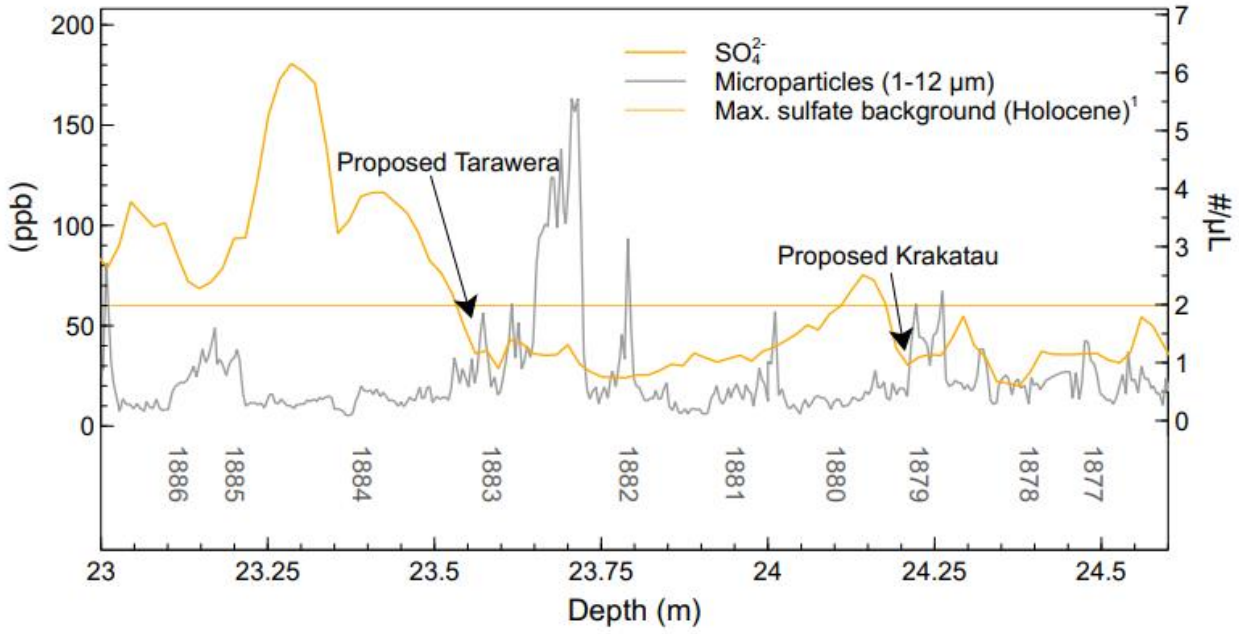


**Figure 2.5.** SPC14 Depth Profile with Proposed Signal Attributions. SPC14 sulfate and microparticle concentration variation with depth and our proposed revisions to the SP19 timescale. We propose that the sulfate signal increase beginning at 23.56 meters depth be reassigned to 1886 CE and the eruption of Tarawera, and that the sulfate signal increase beginning at 24.19 meters depth be reassigned to 1883 CE and the eruption of Krakatau. The proposed Krakatau signal peak (73.5 ppb) remains above the background sulfate maximum of 60 ppb calculated by Winski et al. (2019).

Finally, we consider the identification of Tarawera volcanic products in the 23.61-23.79m depth interval of SPC14 immediately preceding a sulfate spike previously assigned to the 1883 CE eruption of Krakatau, and a possible need to adjust the SP19 timescale at this depth interval. We propose that the age of the sulfate signal increase beginning at 23.56 meters

depth be reassigned to 1886 CE and the eruption of Tarawera (Fig. 5). A small increase in sulfate beginning at 24.19 meters depth likely represents the deposition of volcanic aerosols from the 1883 CE Krakatau eruption and should be reassigned as such. The peak sulfate for the proposed Krakatau signal reaches a maximum concentration of 75.3 ppb at 24.14 meters depth; while small, the signal is still over the background sulfate maximum (median annual) of 60 ppb observed throughout the Holocene (Winski et al., 2019). Because the SP19 timescale was developed, in part, by the correlation of sulfate and ECM time series with the WDC-06A ice core (Fudge et al., 2016), there may be a need to revisit the West Antarctic Ice Sheet (WAIS) Divide ice core timescale "WD2014" (Sigl et al., 2016) as well.

**Conclusions**

By successfully updating the methodology to extract and geochemically characterize tephra from ice cores, we discovered a rhyolitic cryptotephra in the 23.61-23.79 meters depth section of the South Pole ice core (SPC14), currently dated 1882 CE (± 1yr) (see SP19 timescale, Winski et al., 2019).

Measured with EDS, the geochemical composition of cryptotephra is similar to both the most highly evolved products of the 1883 CE eruption of Krakatau, Indonesia, and the 1886 CE eruption of Tarawera, Okataina Volcanic Center, New Zealand. However, the identification of volcanic glass shards as large as 10 µm in the sampling interval cryptotephra favors a regional volcanic source and rapid (within weeks) tropospheric transport similar to the volcanic clouds of the 2011 eruption of Puyehue-Cordón Caulle, Chile (Koffman et al., 2017) to Antarctica.

Thus, we suggest the 1886 CE eruption of Tarawera of the Okataina Volcanic Center as the source of the rhyolitic cryptotephra based on the reported EDS-based geochemical

signature, the inferred atmospheric transport pathway, and the reported signature of rhyolitic products from Tarawera. These results point to a previously unidentified stage of the 1886 CE explosive eruption of Tarawera that coincided with favorable atmospheric conditions that transported volcanic material to Antarctica. The potential for long range transport of fine ash from New Zealand to Antarctica should be considered in future New Zealand volcanic hazard assessments, as they may pose a significant threat to regional aviation safety.

For SPC14, we propose the age of the sulfate signal increase beginning at 23.56 meters depth be reassigned to 1886 CE, and the earlier sulfate increase at 24.14 meters depth be reassigned to 1883 CE.

# CHAPTER 3

## THESIS CONCLUSIONS

This work highlights the utility of ice core tephrochronology and tests the limitations of current and novel methodologies for analyzing ultra-fine tephra (< 10 μm) particles extracted from ice cores. The second chapter of this thesis, as well as data provided in appendices B and D, demonstrate that the current sample processing and mounting techniques used by the University of Maine permit the capture and measurement of ultra-fine tephra particles when present in ice core samples.

Using new sample preparation methods cryptotephra layers were discovered at ~1882 CE, ~1600 CE, ~3518 BCE, ~4526 BCE, ~8127 BCE, and ~9214 BCE of the South Pole Ice Core and ~1628 BCE of the GISP2 (Greenland Ice Sheet Project 2) ice core. Through the consideration of multiple lines of evidence, we infer that the ~1882 CE cryptotephra is likely a product of the 1886 CE Tarawera eruption of the Okataina Volcanic Center. However, as illustrated in the second chapter of this work, current limitations in SEM-EDS analysis of tephra particles < 10 μm in size make for complicated source determinations, especially when potential source eruptions are of similar compositions.

My contribution to Pearson et al., (2022) helped to conclude that the Aniakchak II eruption is the volcanic source of the dated 1628 BCE cryptotephra layer discovered in the GISP2 ice core. The accurate source determination of this cryptotephra separated the climatic forcing of the Aniakchak II event and constrained the timing of the infamous Minoan eruption of Santorini.

**BIBLIOGRAPHY**


Baroni, M., et al., (2007). Mass-Independent Sulfur Isotopic Compositions in Stratospheric Volcanic Eruptions. Science 315, 84–87.

Basile, I., et al., (2001). Volcanic layers in Antarctic (Vostok) ice cores: Source identification and atmospheric implications. J. Geophys. Res.

Burke, A., et al., (2019). Stratospheric eruptions from tropical and extra-tropical volcanoes constrained using high-resolution sulfur isotopes in ice cores. Earth and Planetary Science Letters 521.

Carey, R.J., et al., (2007). Contrasting grain size and componentry in complex proximal deposits of the 1886 Tarawera basaltic Plinian eruption. Bull Volcanol 69, 903–926.

Casadevall, T. J., (1994). Volcanic ash and aviation safety: proceedings of the first international symposium on volcanic ash and aviation safety. Vol. 2047. DIANE Publishing.

Cole, J.W., et al., (1970). Volcanic and structural evolution of the Okataina Volcanic Centre; dominantly silicic volcanism associated with the Taupo Rift, New Zealand. Journal of Volcanology and Geothermal Research 190, 123–135.

Cole-Dai, J., et al., (2000). A 4100-year record of explosive volcanism from an East Antarctica ice core. J. Geophys. Res. 105, 24431–24441.

Coulter, S.E., et al., (2012). Holocene tephras highlight complexity of volcanic signals in Greenland ice cores: HOLOCENE TEPHRAS IN GREENLAND ICE CORES. J. Geophys. Res.

Delmas, R.J., et al., (1992). 1000 years of explosive volcanism recorded at the South Pole. null 44, 335–350.

Dunbar, N.W., et al., (2017). New Zealand supereruption provides time marker for the Last Glacial Maximum in Antarctica. Sci Rep 7, 12238.

Dunbar, N.W., and Kurbatov, A.V., (2011). Tephrochronology of the Siple Dome ice core, West Antarctica: correlations and sources. Quaternary Science Reviews 30, 1602–1614.

Dunbar, N.W., McIntosh, W.C., and Esser, R.P., (2008). Physical setting and tephrochronology of the summit caldera ice record at Mount Moulton, West Antarctica. GSA Bulletin 120, 796–812.

Dunbar, N.W., Zielinski, G., and Voisins, D.T., (2003). Tephra layers in the Siple Dome and Taylor Dome ice cores, Antarctica: Sources and correlations. J. Geophys. Res. 108, 2374.

Esper, J., Schneider, L., and Krusic, P., (2013). European summer temperature response to annually dated volcanic eruptions over the past nine centuries. Bull Volcanol. 75:736.

Fudge, T.J., et al., (2016). Electrical stratigraphy of the WAIS Divide ice core: Identification of centimeter-scale irregular layering. Journal of Geophysical Research: Earth Surface 121, 1218–1229.

Global Volcanism Program, 2013. Volcanoes of the World, v. 4.10.3 (Oct 2021). Venzke, E (ed.). Smithsonian Institution. Downloaded 28 Oct 2021.

Goldstein, J.I., et al., (2018). Scanning Electron Microscopy and X-Ray Microanalysis. Springer New York, New York, NY.

Guffanti, M., Casadevall, T.J., and Budding, K., (2010). Encounters of aircraft with volcanic ash clouds; A compilation of known incidents, 1953-2009 (USGS Numbered Series No. 545), Encounters of aircraft with volcanic ash clouds; A compilation of known incidents, 1953-2009, Data Series. U.S. Geological Survey.

Hall, M.L., et al., (1999). Tungurahua Volcano, Ecuador: structure, eruptive history and hazards. Journal of Volcanology and Geothermal Research 91, 1–21.

Hammer, C.U., Clausen, H.B., and Dansgaard, W., (1980). Greenland ice sheet evidence of post-glacial volcanism and its climatic impact. Nature 288, 230–235.

Hartman, L.H., et al., (2019). Volcanic glass properties from 1459 C.E. volcanic event in South Pole ice core dismiss Kuwae caldera as a potential source. Sci Rep 9, 14437.

Helmick, M., Kurbatov, A. V., Yates, M., 2022. Glass chemistry of cryptotephra extracted from 23.61-23.69m depth of South Pole Ice Core, Version 1.0. Interdisciplinary Earth Data Alliance (IEDA). https://doi.org/10.26022/IEDA/112288

Hopkins, J.L., et al., (2021). TephraNZ: a major- and trace-element reference dataset for glass-shard analyses from prominent Quaternary rhyolitic tephras in New Zealand and implications for correlation. Geochronology 3, 465–504.

Hughes, E., et al., (2021). Magmatic architecture below the Okataina Volcanic Centre, Taupō Volcanic Zone, Aotearoa New Zealand, inferred from basalt geochemistry (preprint). Physical Sciences and Mathematics.

Iverson, N.A., et al., (2017). Advancements and best practices for analysis and correlation of tephra and cryptotephra in ice. Quaternary Geochronology 40, 45–55.

Jiang, S., et al., (2012). A detailed 2840 year record of explosive volcanism in a shallow ice core from Dome A, East Antarctica. J. Glaciol. 58, 65–75.

Keam, R.F., (2016). The Tarawera eruption, Lake Rotomahana, and the origin of the Pink and White Terraces. Journal of Volcanology and Geothermal Research 314, 10–38.

Koffman, B.G., et al., (2017). Rapid transport of ash and sulfate from the 2011 Puyehue-Cordón Caulle (Chile) eruption to West Antarctica: Puyehue Transport to West Antarctica. J. Geophys. Res. Atmos. 122, 8908–8920.

Kuehn, S.C., and Froese, D.G. (2010). Tephra from Ice-A Simple Method to Routinely Mount, Polish, and Quantitatively Analyze Sparse Fine Particles. Microsc. Microanal. 16:218-225.

Kurbatov, A.V., et al., (2006). A 12,000 year record of explosive volcanism in the Siple Dome Ice Core, West Antarctica. J. Geophys. Res. 111, D12307.

Lemieux-Dudon, et al., (2010). Consistent dating for Antarctic and Greenland ice cores. Quaternary Science Reviews 29, 8–20.

Leonard, G.S., et al., (2002). Basalt triggering of the c. AD 1305 Kaharoa rhyolite eruption, Tarawera Volcanic Complex, New Zealand. Journal of Volcanology and Geothermal Research 115, 461–486.

Lilien, D. A. et al. Holocene Ice-Flow Speedup in the Vicinity of the South Pole. Geophysical Research Letters 45, 6557–6565 (2018).

Lowe, D.J., et al., (2017). Correlating tephras and cryptotephras using glass compositional analyses and numerical and statistical methods: Review and evaluation. Quaternary Science Reviews 175, 1–44.

Madden-Nadeau, A., 2020. Geochemical and petrological data pertaining to the eruptive deposits of 1883 caldera-forming eruption of Krakatau. https://doi.org/10.5285/AD2A4FA0-7B66-4EC5-A5CF-D78944716EC4

Madden-Nadeau, A.L., et al., (2021). The magmatic and eruptive evolution of the 1883 caldera-forming eruption of Krakatau: Integrating field- to crystal-scale observations. Journal of Volcanology and Geothermal Research 411,

Mandeville, C.W., Carey, S., and Sigurdsson, H., 1996. Magma mixing, fractional crystallization and volatile degassing during the 1883 eruption of Krakatau volcano, Indonesia. Journal of Volcanology and Geothermal Research 74, 243–274.

Matsuoka, K., et al., (2021). Quantarctica, an integrated mapping environment for Antarctica, the Southern Ocean, and sub-Antarctic islands. Environmental Modelling & Software 140, 105015.

McConnell, J.R., et al., (2020). Extreme climate after massive eruption of Alaska's Okmok volcano in 43 BCE and effects on the late Roman Republic and Ptolemaic Kingdom. Proceedings of the National Academy of Sciences, 117(27), pp. 15443–15449.

Nairn, I.A., (1979). Rotomahana—Waimangu eruption, 1886: base surge and basalt magma. New Zealand Journal of Geology and Geophysics 22, 363–378.

Narcisi, B., Petit, J.R., Chappellaz, J., (2010). A 70 ka record of explosive eruptions from the TALDICE ice core (Talos Dome, East Antarctic plateau). J. Quaternary Sci. 25, 844–849.

Narcisi, B., et al., (2005). Characteristics and sources of tephra layers in the EPICA-Dome C ice record (East Antarctica): Implications for past atmospheric circulation and ice core stratigraphic correlations. Earth and Planetary Science Letters 239, 253–265.

Narcisi, B., et al., (2012). A 16,000-yr tephra framework for the Antarctic ice sheet: a contribution from the new Talos Dome core. Quaternary Science Reviews 49, 52–63.

Narcisi, B., Petit, J.R., and Langone, A., (2017). Last glacial tephra layers in the Talos Dome ice core (peripheral East Antarctic Plateau), with implications for chronostratigraphic correlations and regional volcanic history. Quaternary Science Reviews 165, 111–126.

Newnham, R.M., et al., (1998). The Kaharoa Tephra as a Critical Datum for Earliest Human Impact in Northern New Zealand. Journal of Archaeological Science 25, 533–544.

Palais, J.M., Kirchner, S., Delmas, R.J., (1990). Identification of Some Global Volcanic Horizons by Major Element Analysis of Fine Ash in Antarctic Ice. Annals of Glaciology 14, 216–220.

Palais, J.M., et al., (1987). Correlation of a 3,200 year old tephra in ice cores from Vostok and South Pole Stations, Antarctica. Geophysical Research Letters 14, 804–807.

Palmer, A.S., et al., (2001). High-precision dating of volcanic events (A.D. 1301-1995) using ice cores from Law Dome, Antarctica. J. Geophys. Res. 106, 28089–28095.

Pearson, C., et al., (2022). Geochemical ice-core constraints on the timing and climatic impact of Aniakchak II (1628 BCE) and Thera (Minoan) volcanic eruptions. PNAS Nexus 1, pgac048.

Pittari, A., Briggs, R.M., Bowyer, D.A., (2016). Subsurface geology, ancient hydrothermal systems and crater excavation processes beneath Lake Rotomahana: Evidence from lithic clasts of the 1886AD Rotomahana Pyroclastics. Journal of Volcanology and

Geothermal Research, The Lake Rotomahana Geothermal System and Effects of the 1886 Mt. Tarawera Eruption 314, 110–125.

Plummer, C.T., et al., (2012). An independently dated 2000-yr volcanic record from Law Dome, East Antarctica, including a new perspective on the dating of the 1450s CE eruption of Kuwae, Vanuatu. Clim. Past 8, 1929–1940.

Plunkett, G., et al., (2020). Smoking guns and volcanic ash: the importance of sparse tephras in Greenland ice cores. Polar Research 2020, 39, 3511.

Prata, F., Rose, W.I., 2015. Volcanic ash hazards to aviation. The Encyclopedia of Volcanoes, 2nd Edition, 911-934.

Rosseel, J.-B., White, J.D.L., Houghton, B.F., (2006). Complex bombs of phreatomagmatic eruptions: Role of agglomeration and welding in vents of the 1886 Rotomahana eruption, Tarawera, New Zealand. Journal of Geophysical Research: Solid Earth 111.

Rowe, M.C., et al., (2021). Tarawera 1886: an integrated review of volcanological and geochemical characteristics of a complex basaltic eruption. New Zealand Journal of Geology and Geophysics 64, 296–319.

Saalfeld, M.A., 2018. Petrology of the 1877 eruption of Cotopaxi Volcano, Ecuador: Insight on magma evolution and storage. Bowling Green State University.

Sable, J.E., et al., (2009). Eruption mechanisms during the climax of the Tarawera 1886 basaltic Plinian eruption inferred from microtextural characteristics of the deposits.

Self, S., 1992. Krakatau revisited: The course of events and interpretation of the 1883 eruption. GeoJournal 28.

Self, S., Rampino, M.R., 1981. The 1883 eruption of Krakatau. Nature 294, 699–704.

Sigl, M., et al., (2013). A new bipolar ice core record of volcanism from WAIS Divide and NEEM and implications for climate forcing of the last 2000 years: A 2000yr bipolar volcano record. J. Geophys. Res. Atmos. 118, 1151–1169.

Sigl, M., et al., (2015). Timing and climate forcing of volcanic eruptions for the past 2,500 years. Nature 523, 543–549.

Sigl, M., et al., (2016). The WAIS Divide deep ice core WD2014 chronology – Part 2: Annual-layer counting (0–31 ka BP). Clim. Past 12, 769–786.

Souney, J.M., et al., (2021). Core handling, transportation and processing for the South Pole ice core (SPICEcore) project. Annals of Glaciology 62, 118–130.

Stehn, C.E., (1929). Krakatau: The geology and volcanism of the Krakatau group. Batavia. Proc. Fourth Pacif. Sci. Congr. Guidebook, 1–55 (1929)

Stenchikov, G., (2021). The role of volcanic activity in climate and global changes, in: Climate Change. Elsevier, pp. 607–643

Taylor, P.W., (1991). The geology and petrology of Niuafo'ou Island, Tonga: subaerial volcanism in an active back-arc basin (thesis). Macquarie University.

Toohey, M., Sigl, M., (2017). Volcanic stratospheric sulfur injections and aerosol optical depth from 500 BCE to 1900 CE. Earth Syst. Sci. Data 9, 809–831.

Turney, C.S.M., et al., (2020). Early Last Interglacial ocean warming drove substantial ice mass loss from Antarctica. Proceedings of the National Academy of Sciences 117, 3996–4006.

Vinther, B.M., et al., (2006). A synchronized dating of three Greenland ice cores throughout the Holocene. J. Geophys. Res. 111, D13102.

Walker, G.P.L., Self, S., Wilson, L., (1984). Tarawera 1886, New Zealand — A basaltic plinian fissure eruption. Journal of Volcanology and Geothermal Research 21, 61–78.

Wallace, K., et al., (2022). Community Established Best Practice Recommendations for Tephra Studies-from Collection through Analysis (forthcoming). Scientific Data: SDATA-21-00892A.

Westerveld, J., (1952). Quaternary volcanism on Sumatra. GSA Bulletin 63, 561–594.

Wilson, C.J.N., et al., (1995). Volcanic and structural evolution of Taupo Volcanic Zone, New Zealand: a review. Journal of Volcanology and Geothermal Research, Taupo Volcanic Zone, New Zealand 68, 1–28.

Winski, D. A. (2021) "South Pole Ice Core Holocene Major Ion Dataset" U.S. Antarctic Program (USAP) Data Center. doi: https://doi.org/10.15784/601399.

Winski, D.A., et al., (2019). The SP19 chronology for the South Pole Ice Core – Part 1: volcanic matching and annual layer counting. Clim. Past 15, 1793–1808.

Zdanowicz, C.M., Zielinski, G.A., and Germani, M.S., (1999). Mount Mazama eruption: Calendrical age verified and atmospheric impact assessed. Geology 27, 621–624.

Zielinski, G.A., (2000). Use of paleo-records in determining variability within the volcanism–climate system. Quaternary Science Reviews 19, 417–438.

Zielinski, G.A., (1995). Stratospheric loading and optical depth estimates of explosive volcanism over the last 2100 years derived from the Greenland Ice Sheet Project 2 ice core. J. Geophys. Res. 100, 20937.

Zielinski, G.A., et al., (1997). Volcanic aerosol records and tephrochronology of the Summit, Greenland, ice cores. J. Geophys. Res. 102, 26625–26640.

# APPENDICES

## APPENDIX A: CHAPTER 2 SUPPLEMENTARY DATA

**Table A.1.** SPC14 Subsampled Volcanic Intervals Investigated for Cryptotephra Reported in Chapter 2

| Depth Interval (m) | Year (CE)[1] | Peak Sulfate (ppb)[2] | Tephra Detected |
|---|---|---|---|
| 22.9-23.0 | 1887.4-1886.6 | 85.47 | No |
| 23.0-23.15 | 1886.6-1885.3 | 111.8 | No |
| 23.15-23.38 | 1885.3-1883.9 | 180.6 | No |
| 23.38-23.61 | 1883.9-1882.7 | 116.4 | No |
| 23.61-23.79 | 1882.7-1881.8 | 42.89 | Yes |
| 23.79-23.95 | 1881.8-1880.8 | 36.28 | No |
| 24.0-24.05 | 1880.5-1880.1 | 45.82 | No |
| 24.05-24.20 | 1880.1-1879.0 | 75.33 | No |

1. Winski et al. (2019)
2. Winski, D. A. (2021)

**Table A.2**. UMaine SEM-EDS Instrument and Session Specifications

| | |
|---|---|
| **Sample ID** | SPC14 23.61-23.79m |
| **Lab Sample** | AntT 483 |
| **Ice core** | South Pole Ice Core (SPC14) |
| **Depth** | 23.61-23.79m |
| **Coating** | 15 nm, carbon |
| **Analyzed as reference material** | No |
| **Target Material Analyzed** | volcanic glass shards |
| **Data Line Type** | Single |
| **Analyst** | MEH |
| **Method** | UMaine Tephra SEM-EDS 20210819 |
| **Technique** | SEM-EDS |
| **Instrument** | Tescan Vega II XMU |
| **Detector** | Apollo40 SSD |
| **Lab Information** | Electron Microscopy Laboratory, The University of Maine, https://umaine.edu/earthclimate/facilities/electron-microscopy-laboratory/ |
| **Beam Conditions** | 15 kV, 120 nA, focused beam |
| **Acquisition Time (seconds)** | 100 (session 1 and 2), 200 (session 3) |
| **Secondary Reference Materials** | Old Crow Tephra, ATHO-G (See Table A4). |
| **EDS Utilized?** | Yes |
| **EDS Software** | EDAX Genesis v6.1 |
| **Oxide Calculation Procedure** | EDAX Genesis v6.1 PhiRhoZ and USNM 72854 VG-568 rhyolitic glass standard |
| **EDS PC OS** | Windows XP |

**Table A.3.** Major elemental composition of particles extracted from the SPC14 23.61-23.79 sample depth of the South Pole Ice Core. Geochemical data is calculated using EDAX Genesis quantification procedure with NMNH 72854 Rhyolite Glass standard. All data were collected under SEM-EDS operating conditions found in Table B.2. unless otherwise specified. All measurements are in weight percent oxide and are normalized to 100% weight percent. Analytical accuracy and precision, based on replicate analysis of three standard reference materials, are presented in Table A.4. Average precision is also listed as a footnote in this table.

| Session | $Na_2O$ (wt.%) | MgO (wt.%) | $Al_2O_3$ (wt.%) | $SiO_2$ (wt.%) | $P_2O_5$ (wt.%) | $K_2O$ (wt.%) | CaO (wt.%) | $TiO_2$ (wt.%) | MnO (wt.%) | FeO (wt.%) | Grain Size (µm) | Comment |
|---|---|---|---|---|---|---|---|---|---|---|---|---|
| 1 | 4.84 | 0.34 | 13.58 | 74.53 | 0 | 2.63 | 1.52 | 0.34 | 0.04 | 2.18 | 4 | unpolished |
| 1 | 3.23 | 0.18 | 10.97 | 79.04 | 0.6 | 3.44 | 0.73 | 0.33 | 0.02 | 1.46 | 6 | unpolished |
| 1 | 3.93 | 0.2 | 12.41 | 77.24 | 0 | 3.42 | 1.34 | 0.25 | 0.02 | 1.17 | 10 | unpolished |
| 1 | 3.67 | 0.18 | 12.12 | 77.03 | 0.64 | 3.44 | 1.17 | 0.34 | 0.02 | 1.39 | 10 | unpolished |
| 1 | 4.19 | 0.31 | 13.99 | 75.18 | 0 | 2.44 | 1.55 | 0.29 | 0 | 2.05 | 4 | unpolished |
| 1 | 2.36 | 0.28 | 14.35 | 76.29 | 0.07 | 2.55 | 1.61 | 0.31 | 0.02 | 2.16 | 4 | unpolished |
| **Average** | **3.7** | **0.2** | **12.9** | **76.6** | **0.2** | **3.0** | **1.3** | **0.3** | **0.0** | **1.7** | | |
| *Std.Dev* | *0.8* | *0.1* | *1.2* | *1.5* | *0.3* | *0.5* | *0.3* | *0.0* | *0.0* | *0.4* | | |
| 2 | 2.7 | 0.15 | 12.68 | 76.68 | 0 | 3.53 | 1.86 | 0.36 | 0.12 | 1.93 | 3 | polished |
| 2 | 2.61 | 0.28 | 12.22 | 77.96 | 0.31 | 3.4 | 1.43 | 0 | 0.09 | 1.7 | 4 | polished |
| 2 | 3.03 | 0.28 | 11.95 | 77.09 | 0.52 | 3.82 | 1.15 | 0.21 | 0.08 | 1.87 | 3 | polished |
| 2 | 2.67 | 0.12 | 11.16 | 78.16 | 0.32 | 4.61 | 0.53 | 0.37 | 0.07 | 1.99 | 2.5 | polished |
| 2 | 2.48 | 0.37 | 12.77 | 77.41 | 0.3 | 3.31 | 1.52 | 0.2 | 0.06 | 1.57 | 4 | polished |
| 2 | 2.85 | 0.08 | 11.03 | 79.59 | 0 | 3.57 | 1.06 | 0.23 | 0.05 | 1.54 | 3 | polished |
| 2 | 4.55 | 0.12 | 16.23 | 71.18 | 0.22 | 2.29 | 3.8 | 0.2 | 0.04 | 1.4 | 3 | polished |
| **Average** | **3.0** | **0.2** | **12.0** | **77.8** | **0.2** | **3.7** | **1.3** | **0.2** | **0.1** | **1.8** | | |
| *Std.Dev* | *0.2* | *0.1* | *0.7* | *0.9* | *0.2* | *0.4* | *0.4* | *0.1* | *0.0* | *0.2* | | |

*Note: Analytical precision, based on replicate analyses of rhyolitic reference material, are as follows for each session (all in wt.%):*

*Session 1: $Na_2O$±0.71, MgO± 0.03, $Al_2O_3$± 0.09, $SiO_2$±1.05, $P_2O_5$±0.00, $K_2O$±0.11, CaO±0.13, $TiO_2$±0.18, MnO±0.05, FeO±0.14.*

*Session 2: $Na_2O$±0.57, MgO± 0.11, $Al_2O_3$± 0.27, $SiO_2$±0.19, $P_2O_5$±0.03, $K_2O$±0.16, CaO±0.23, $TiO_2$±0.11, MnO±0.01, FeO±0.11.*

**Table A.3**. SPC14 Glass Geochemistry (23.61-23.79 sample depth) (continued).

| Session | $Na_2O$ (wt.%) | MgO (wt.%) | $Al_2O_3$ (wt.%) | $SiO_2$ (wt.%) | $P_2O_5$ (wt.%) | $K_2O$ (wt.%) | CaO (wt.%) | $TiO_2$ (wt.%) | MnO (wt.%) | FeO (wt.%) | Grain Size (µm) | Comment |
|---|---|---|---|---|---|---|---|---|---|---|---|---|
| 3 | 1.15 | 0.13 | 12.49 | 77.01 | 1 | 4.77 | 0.84 | 0.18 | 0.75 | 1.66 | 2 | polished |
| 3 | 2.32 | 0.15 | 11.61 | 77.07 | 0.68 | 3.3 | 0.96 | 0.23 | 0.81 | 2.86 | 3 | polished |
| 3 | 2.82 | 0.15 | 12.43 | 77.31 | 0 | 3.65 | 1.28 | 0.2 | 0.3 | 1.86 | 4 | polished |
| 3 | 2.97 | 0.22 | 12.74 | 75.81 | 0.49 | 3.31 | 1.33 | 0.14 | 0.47 | 2.51 | 2.5 | polished |
| 3 | 2.07 | 0.12 | 10.42 | 79.89 | 0 | 3.08 | 0.85 | 0.29 | 0.99 | 2.29 | 1.5 | polished |
| 3 | 2.28 | 0.11 | 12.16 | 77.37 | 1.08 | 3.35 | 0.85 | 0.16 | 0.48 | 2.15 | 2.6 | polished |
| 3 | 1.95 | 0.08 | 11.56 | 78.92 | 1.02 | 3.46 | 0.73 | 0.2 | 0.51 | 1.58 | 2 | polished |
| **Average** | **2.2** | **0.1** | **11.9** | **77.6** | **0.6** | **3.6** | **1.0** | **0.2** | **0.6** | **2.1** | | |
| *Std.Dev* | *0.6* | *0.0* | *0.7* | *1.3* | *0.4* | *0.5* | *0.2* | *0.0* | *0.2* | *0.4* | | |

*Note: Analytical precision, based on replicate analyses of rhyolitic reference material, are as follows for each session (all in wt.%):*

*Session 3: $Na_2O$±0.66, MgO± 0.06, $Al_2O_3$± 0.11, $SiO_2$±0.74, $P_2O_5$±0.13, $K_2O$±0.06, CaO±0.02, $TiO_2$±0.01, MnO±0.21, FeO±0.05.*

**Table A.4**. Major elemental analyses of reference materials performed during each SEM-EDS analytical session. Secondary references values represent averages of "N" analyses, and all values are reported as weight percent oxide and are normalized to 100% weight percent.

| Reference Material | N | $Na_2O$ (wt.%) | MgO (wt.%) | $Al_2O_3$ (wt.%) | $SiO_2$ (wt.%) | $P_2O_5$ (wt.%) | $K_2O$ (wt.%) | CaO (wt.%) | $TiO_2$ (wt.%) | MnO (wt.%) | FeO (wt.%) | Instrument |
|---|---|---|---|---|---|---|---|---|---|---|---|---|
| Old Crow Tephra | 3 | 3.14 | 0.14 | 12.94 | 75.96 | 0.00 | 3.89 | 1.46 | 0.75 | 0.09 | 1.63 | SEM-EDS |
| std.dev | | 0.71 | 0.03 | 0.09 | 1.05 | 0.00 | 0.11 | 0.13 | 0.18 | 0.05 | 0.14 | Method 1 |
| Reference Value* | | 3.83 | 0.29 | 13.08 | 75.47 | 0.04 | 3.73 | 1.5 | 0.31 | 0.05 | 1.69 | |
| ATHO-G | 4 | 5.04 | 0.36 | 12.2 | 75.76 | 0.04 | 2.86 | 2.03 | 0.32 | 0.07 | 1.35 | SEM-EDS |
| std.dev | | 0.57 | 0.11 | 0.27 | 0.19 | 0.03 | 0.16 | 0.23 | 0.11 | 0.01 | 0.11 | Method 2 |
| Reference Value* | | 3.75 | 0.103 | 12.2 | 75.6 | 0.025 | 2.64 | 1.7 | 0.255 | 0.106 | 3.27 | |
| ATHO-G | 3 | 2.63 | 0.07 | 12.34 | 76.37 | 0.13 | 2.81 | 1.3 | 0.18 | 0.52 | 3.66 | SEM-EDS |
| std.dev | | 0.66 | 0.06 | 0.11 | 0.74 | 0.13 | 0.06 | 0.02 | 0.1 | 0.21 | 0.05 | Method 3 |
| Reference Value* | | 3.75 | 0.103 | 12.2 | 75.6 | 0.025 | 2.64 | 1.7 | 0.255 | 0.106 | 3.27 | |

*Kuehn et al. (2011)

## APPENDIX B: SOUTH POLE ICE CORE TEPHROSTRATIGRAPHY

**Table B.1**. Major elemental composition of particles extracted from the South Pole Ice Core. Geochemical data is calculated using EDAX Genesis quantification procedure with NMNH 72854 Rhyolite Glass standard. All data were collected under SEM-EDS operating conditions found in Table B.2. unless otherwise specified. All measurements are in weight percent oxide and are normalized to 100% weight percent. Analytical accuracy and precision, based on replicate analysis of rhyolitic and basaltic reference materials, are presented as a footnote in this table.

| AntT ID: | 478 | | $Na_2O$ | MgO | $Al_2O_3$ | $SiO_2$ | $P_2O_5$ | $K_2O$ | CaO | $TiO_2$ | MnO | FeO |
|---|---|---|---|---|---|---|---|---|---|---|---|---|
| Depth (m) | 6.5-6.8 | | 1.82 | 1.42 | 17.06 | 66.33 | 0.58 | 2.6 | 1.21 | 3.4 | 0.18 | 5.41 |
| Age (CE) | 1983-1984 | | | | | | | | | | | |
| Target Event: | N/A | | | | | | | | | | | |
| AntT ID: | 469 | | $Na_2O$ | MgO | $Al_2O_3$ | $SiO_2$ | $P_2O_5$ | $K_2O$ | CaO | $TiO_2$ | MnO | FeO |
| Depth (m) | 10-10.17 | | 6.05 | 0.24 | 11.34 | 71.24 | 0.85 | 6.07 | 1.02 | 0.64 | 1.2 | 1.34 |
| Age (CE) | 1965-1966 | | 4.33 | 0.22 | 16.5 | 61.7 | 0.62 | 12.45 | 0.91 | 0.65 | 1.09 | 1.53 |
| Target Event: | Agung | *avg.* | *5.19* | *0.23* | *13.92* | *66.47* | *0.74* | *9.26* | *0.97* | *0.65* | *1.15* | *1.44* |
| | | *stdev.* | *1.22* | *0.01* | *3.65* | *6.75* | *0.16* | *4.51* | *0.08* | *0.01* | *0.08* | *0.13* |
| AntT ID: | 470 | | $Na_2O$ | MgO | $Al_2O_3$ | $SiO_2$ | $P_2O_5$ | $K_2O$ | CaO | $TiO_2$ | MnO | FeO |
| Depth (m) | 10.17-10.38 | | 1.78 | 1.43 | 10.09 | 69.63 | - | 2.28 | 6.55 | 0.37 | 0.14 | 7.74 |
| Age (CE) | 1963-1965 | | | | | | | | | | | |
| Target Event: | Agung | | | | | | | | | | | |

**Table B.1**. Continued.

| AntT ID: | 472 | | $Na_2O$ | MgO | $Al_2O_3$ | $SiO_2$ | $P_2O_5$ | $K_2O$ | CaO | $TiO_2$ | MnO | FeO |
|---|---|---|---|---|---|---|---|---|---|---|---|---|
| Depth (m) | 10.59-10.80 | | 0.76 | 2.02 | 16.87 | 67.87 | 0 | 0.59 | 1.29 | 0.81 | 0.66 | 9.14 |
| Age (CE) | 1962-1963 | | | | | | | | | | | |
| Target Event: | Agung | | | | | | | | | | | |
| AntT ID: | 480 | | $Na_2O$ | MgO | $Al_2O_3$ | $SiO_2$ | $P_2O_5$ | $K_2O$ | CaO | $TiO_2$ | MnO | FeO |
| Depth (m) | 23-23.15 | | 0.11 | 0.55 | 13.38 | 77.01 | 0.31 | 0.46 | 0.91 | 1.41 | 0.14 | 5.73 |
| Age (CE) | 1885-1886 | | 2.36 | 0.31 | 13.51 | 71.72 | 1.2 | 3.47 | 2.17 | 1.52 | 0.18 | 3.55 |
| Target Event: | Tarawera | *avg.* | *1.24* | *0.43* | *13.45* | *74.37* | *0.76* | *1.97* | *1.54* | *1.47* | *0.16* | *4.64* |
| | | *stdev.* | *1.59* | *0.17* | *0.09* | *3.74* | *0.63* | *2.13* | *0.89* | *0.08* | *0.03* | *1.54* |

**Table B.1**. Continued.

| AntT ID: | 483 | | $Na_2O$ | MgO | $Al_2O_3$ | $SiO_2$ | $P_2O_5$ | $K_2O$ | CaO | $TiO_2$ | MnO | FeO |
|---|---|---|---|---|---|---|---|---|---|---|---|---|
| Depth (m) | 23.61-23.79 | | 4.84 | 0.34 | 13.58 | 74.53 | 0 | 2.63 | 1.52 | 0.34 | 0.04 | 2.18 |
| Age (CE) | 1881-1882 | | 3.23 | 0.18 | 10.97 | 79.04 | 0.6 | 3.44 | 0.73 | 0.33 | 0.02 | 1.46 |
| Target Event: | Krakatau | | 3.93 | 0.2 | 12.41 | 77.24 | 0 | 3.42 | 1.34 | 0.25 | 0.02 | 1.17 |
| | | | 3.67 | 0.18 | 12.12 | 77.03 | 0.64 | 3.44 | 1.17 | 0.34 | 0.02 | 1.39 |
| Geochemical data for this sample were obtained via three different methods. | | | 4.19 | 0.31 | 13.99 | 75.18 | 0 | 2.44 | 1.55 | 0.29 | 0 | 2.05 |
| | | | 2.36 | 0.28 | 14.35 | 76.29 | 0.07 | 2.55 | 1.61 | 0.31 | 0.02 | 2.16 |
| | | *avg.* | *3.70* | *0.25* | *12.90* | *76.55* | *0.22* | *2.99* | *1.32* | *0.31* | *0.02* | *1.74* |
| | | *stdev.* | *0.85* | *0.07* | *1.29* | *1.61* | *0.31* | *0.49* | *0.33* | *0.04* | *0.01* | *0.45* |
| Session 1 | | Session 1 (Above) | | | | | | | | | | |
| Normal SEM conditions on unpolished sample | | | 2.7 | 0.15 | 12.68 | 76.68 | 0 | 3.53 | 1.86 | 0.36 | 0.12 | 1.93 |
| | | | 2.61 | 0.28 | 12.22 | 77.96 | 0.31 | 3.4 | 1.43 | 0 | 0.09 | 1.7 |
| Session 2 | | | 3.03 | 0.28 | 11.95 | 77.09 | 0.52 | 3.82 | 1.15 | 0.21 | 0.08 | 1.87 |
| Normal SEM conditions on polished sample | | | 2.67 | 0.12 | 11.16 | 78.16 | 0.32 | 4.61 | 0.53 | 0.37 | 0.07 | 1.99 |
| | | | 2.48 | 0.37 | 12.77 | 77.41 | 0.3 | 3.31 | 1.52 | 0.2 | 0.06 | 1.57 |
| Session 3 | | | 2.85 | 0.08 | 11.03 | 79.59 | 0 | 3.57 | 1.06 | 0.23 | 0.05 | 1.54 |
| Normal SEM conditions at 200 seconds of live time on polished sample | | *avg.* | *2.72* | *0.21* | *11.97* | *77.82* | *0.24* | *3.71* | *1.26* | *0.23* | *0.08* | *1.77* |
| | | *stdev.* | *0.19* | *0.11* | *0.74* | *1.03* | *0.20* | *0.48* | *0.46* | *0.13* | *0.02* | *0.19* |
| | | Session 2 (Above) | | | | | | | | | | |
| | | | 1.15 | 0.13 | 12.49 | 77.01 | 1 | 4.77 | 0.84 | 0.18 | 0.75 | 1.66 |
| | | | 2.32 | 0.15 | 11.61 | 77.07 | 0.68 | 3.3 | 0.96 | 0.23 | 0.81 | 2.86 |
| | | | 2.82 | 0.15 | 12.43 | 77.31 | 0 | 3.65 | 1.28 | 0.2 | 0.3 | 1.86 |
| | | | 2.97 | 0.22 | 12.74 | 75.81 | 0.49 | 3.31 | 1.33 | 0.14 | 0.47 | 2.51 |
| | | | 2.07 | 0.12 | 10.42 | 79.89 | 0 | 3.08 | 0.85 | 0.29 | 0.99 | 2.29 |
| | | | 2.28 | 0.11 | 12.16 | 77.37 | 1.08 | 3.35 | 0.85 | 0.16 | 0.48 | 2.15 |
| | | | 1.95 | 0.08 | 11.56 | 78.92 | 1.02 | 3.46 | 0.73 | 0.2 | 0.51 | 1.58 |
| | | *avg.* | *2.22* | *0.14* | *11.92* | *77.63* | *0.61* | *3.56* | *0.98* | *0.20* | *0.62* | *2.13* |
| | | *stdev.* | *0.60* | *0.04* | *0.79* | *1.35* | *0.47* | *0.56* | *0.23* | *0.05* | *0.24* | *0.47* |
| | | Session 3 (Above) | | | | | | | | | | |

**Table B.1**. Continued.

| AntT ID: | 490 | | $Na_2O$ | MgO | $Al_2O_3$ | $SiO_2$ | $P_2O_5$ | $K_2O$ | CaO | $TiO_2$ | MnO | FeO |
|---|---|---|---|---|---|---|---|---|---|---|---|---|
| Depth (m) | 30-30.11 | | 4.45 | 0.31 | 11.56 | 77.45 | 0.37 | 3.84 | 0.86 | 0.19 | 0.02 | 0.95 |
| Age (CE) | 1840-1841 | | | | | | | | | | | |
| Target Event: | N/A | | | | | | | | | | | |
| AntT ID: | 497 | | $Na_2O$ | MgO | $Al_2O_3$ | $SiO_2$ | $P_2O_5$ | $K_2O$ | CaO | $TiO_2$ | MnO | FeO |
| Depth (m) | 30.70-30.84 | | 0.62 | 1.95 | 14 | 74.88 | - | 0.86 | 0.5 | 0.23 | - | 6.97 |
| Age (CE) | 1834-1835 | | 2.85 | 0.26 | 13.03 | 76.09 | - | 4.42 | 1.11 | 0.22 | - | 2.02 |
| Target Event: | Cosiguina | | 5.51 | 0.75 | 13.81 | 66.49 | - | 0.79 | 3.69 | 0.47 | - | 8.47 |
| | | | 0.81 | 1.61 | 13.83 | 68.43 | - | 1.46 | 0.84 | 0.45 | - | 12.57 |
| | | | 0.85 | 1.13 | 15.14 | 69.01 | - | 1.45 | 3.93 | 5.21 | - | 3.29 |
| | | *avg.* | *2.13* | *1.14* | *13.96* | *70.98* | - | *1.80* | *2.01* | *1.32* | - | *6.66* |
| | | *stdev.* | *2.10* | *0.67* | *0.76* | *4.24* | - | *1.50* | *1.66* | *2.18* | - | *4.22* |
| AntT ID: | 504 | | $Na_2O$ | MgO | $Al_2O_3$ | $SiO_2$ | $P_2O_5$ | $K_2O$ | CaO | $TiO_2$ | MnO | FeO |
| Depth (m) | 31.06-31.19 | | 0.85 | 1.13 | 15.14 | 69.01 | - | 1.45 | 3.93 | 5.21 | - | 3.29 |
| Age (CE) | 1831-1832 | | | | | | | | | | | |
| Target Event: | Babuyan | | | | | | | | | | | |
| AntT ID: | 489 | | $Na_2O$ | MgO | $Al_2O_3$ | $SiO_2$ | $P_2O_5$ | $K_2O$ | CaO | $TiO_2$ | MnO | FeO |
| Depth (m) | 32.93-32.99 | | 3.52 | 0.19 | 12.53 | 75.69 | 0.73 | 4.68 | 0.64 | 0.65 | 0.15 | 1.23 |
| Age (CE) | 1815-1816 | | | | | | | | | | | |
| Target Event: | Tambora | | | | | | | | | | | |

**Table B.1**. Continued.

| AntT ID: | 506 | | $Na_2O$ | MgO | $Al_2O_3$ | $SiO_2$ | $P_2O_5$ | $K_2O$ | CaO | $TiO_2$ | MnO | FeO |
|---|---|---|---|---|---|---|---|---|---|---|---|---|
| Depth (m) | 33.12-33.19 | | 7.72 | 0.28 | 18.1 | 63.32 | 0.72 | 4.26 | 3.09 | 0.31 | 0.02 | 2.17 |
| Age (CE) | 1814 | | 8.78 | 0.94 | 17.54 | 59.74 | 0.31 | 6.09 | 2.12 | 0.5 | 0.04 | 3.94 |
| Target Event: | Tambora | | 2.94 | 0.59 | 17.14 | 66.14 | 0.74 | 9.33 | 0.51 | 0.35 | 0.02 | 2.23 |
| | | | 7.01 | 0.66 | 16.77 | 60.14 | 0.74 | 5.5 | 2.99 | 0.47 | 0.03 | 5.7 |
| | | | 5.08 | 0.27 | 19.1 | 61.45 | - | 6.98 | 1.98 | 0.61 | - | 4.53 |
| | | | 4.84 | 0.07 | 17.03 | 64.38 | - | 7.55 | 1.26 | 0.27 | - | 4.59 |
| | | | 4.69 | 0.63 | 16.26 | 59.94 | - | 4.79 | 2.83 | 0.87 | - | 9.98 |
| | | *avg.* | *5.87* | *0.49* | *17.42* | *62.16* | *0.63* | *6.36* | *2.11* | *0.48* | *0.03* | *4.73* |
| | | *stdev.* | *2.04* | *0.30* | *0.94* | *2.50* | *0.21* | *1.75* | *0.96* | *0.21* | *0.01* | *2.65* |
| AntT ID: | 507 | | $Na_2O$ | MgO | $Al_2O_3$ | $SiO_2$ | $P_2O_5$ | $K_2O$ | CaO | $TiO_2$ | MnO | FeO |
| Depth (m) | 33.19-33.32 | | 5.14 | 0.09 | 11.54 | 75.61 | 0.32 | 4.65 | 0.64 | 0.28 | 0.05 | 1.67 |
| Age (CE) | 1813-1814 | | 4.19 | 0.39 | 13.81 | 73.14 | 1.28 | 1.64 | 1.95 | 0.52 | 0.06 | 3.02 |
| Target Event: | Tambora | | 7.41 | 0.74 | 15.91 | 64.16 | 2.13 | 4.49 | 0.7 | 0.49 | 0.03 | 3.93 |
| | | | 9.12 | 0.69 | 14.83 | 63.7 | 1.63 | 4.96 | 0.28 | 0.08 | 0 | 4.7 |
| | | *avg.* | *6.47* | *0.48* | *14.02* | *69.15* | *1.34* | *3.94* | *0.89* | *0.34* | *0.04* | *3.33* |
| | | *stdev.* | *2.23* | *0.30* | *1.86* | *6.12* | *0.76* | *1.54* | *0.73* | *0.21* | *0.03* | *1.30* |
| AntT ID: | 511 | | $Na_2O$ | MgO | $Al_2O_3$ | $SiO_2$ | $P_2O_5$ | $K_2O$ | CaO | $TiO_2$ | MnO | FeO |
| Depth (m) | 33.71-33.86 | | 4.4 | 0.32 | 11.6 | 77.62 | - | 3.46 | 0.82 | 0.31 | - | 1.46 |
| Age (CE) | 1809-1810 | | | | | | | | | | | |
| Target Event: | 1809 | | | | | | | | | | | |
| AntT ID: | 512 | | $Na_2O$ | MgO | $Al_2O_3$ | $SiO_2$ | $P_2O_5$ | $K_2O$ | CaO | $TiO_2$ | MnO | FeO |
| Depth (m) | 33.86-33.98 | | 4.46 | 0.6 | 12.91 | 62.55 | | 4.08 | 3.78 | 0.6 | | 11.03 |
| Age (CE) | 1808-1809 | | 2.97 | 1.25 | 16.4 | 59.73 | | 5.8 | 0.86 | 1.42 | | 11.56 |
| Target Event: | 1809 | | 4.61 | 0.34 | 10.18 | 68.09 | | 6.46 | 1.23 | 1.92 | | 7.17 |
| | | *avg.* | *4.01* | *0.73* | *13.16* | *63.46* | - | *5.45* | *1.96* | *1.31* | - | *9.92* |
| | | *stdev.* | *0.91* | *0.47* | *3.12* | *4.25* | - | *1.23* | *1.59* | *0.67* | - | *2.40* |

**Table B.1**. Continued.

| AntT ID: | 541 | | $Na_2O$ | MgO | $Al_2O_3$ | $SiO_2$ | $P_2O_5$ | $K_2O$ | CaO | $TiO_2$ | MnO | FeO |
|---|---|---|---|---|---|---|---|---|---|---|---|---|
| Depth (m) | 47.34-47.49 | | 5.38 | 1.86 | 16.66 | 55.86 | 0.5 | 5.29 | 1.68 | 0.78 | 0.34 | 11.66 |
| Age (CE) | 1698-1700 | | 2.95 | 0.13 | 12.57 | 77.18 | 0.95 | 3.93 | 0.79 | 0 | 0.06 | 1.44 |
| Target Event: | N/A | | 4.07 | 0.35 | 15.58 | 70.23 | 0.21 | 1.6 | 3.81 | 0.54 | 0.09 | 3.52 |
| | | *avg.* | *4.13* | *0.78* | *14.94* | *67.76* | *0.55* | *3.61* | *2.09* | *0.44* | *0.16* | *5.54* |
| | | *stdev.* | *1.22* | *0.94* | *2.12* | *10.87* | *0.37* | *1.87* | *1.55* | *0.40* | *0.15* | *5.40* |
| AntT ID: | 530 | | $Na_2O$ | MgO | $Al_2O_3$ | $SiO_2$ | $P_2O_5$ | $K_2O$ | CaO | $TiO_2$ | MnO | FeO |
| Depth (m) | 48.00-48.10 | | 5.61 | 0.6 | 18.92 | 60.09 | 0.87 | 0.95 | 6.61 | 0.52 | 0 | 5.84 |
| Age (CE) | 1693-1694 | | | | | | | | | | | |
| Target Event: | N/A | | | | | | | | | | | |
| AntT ID: | 537 | | $Na_2O$ | MgO | $Al_2O_3$ | $SiO_2$ | $P_2O_5$ | $K_2O$ | CaO | $TiO_2$ | MnO | FeO |
| Depth (m) | 50.37-50.41 | | 4.85 | 1.13 | 13.16 | 66.82 | 0.26 | 5.88 | 4.58 | 0.52 | 0.23 | 2.57 |
| Age (CE) | 1671 | | 2.69 | 2.16 | 13.43 | 69.58 | 0.62 | 4.88 | 1.03 | 0.36 | 0.23 | 5.02 |
| Target Event: | Gamkonora | | 2.81 | 0.18 | 13.61 | 75.44 | 0.25 | 3.15 | 1.49 | 0.34 | 0.18 | 2.56 |
| | | | 3.9 | 0.11 | 13.59 | 75.22 | 0.22 | 3.05 | 1.66 | 0.15 | 0.18 | 1.91 |
| | | | 3.31 | 0.07 | 13.69 | 75.51 | 0 | 2.95 | 1.79 | 0.43 | 0.22 | 2.02 |
| | | *avg.* | *3.51* | *0.73* | *13.50* | *72.51* | *0.27* | *3.98* | *2.11* | *0.36* | *0.21* | *2.82* |
| | | *stdev.* | *0.89* | *0.91* | *0.21* | *4.06* | *0.22* | *1.33* | *1.41* | *0.14* | *0.03* | *1.27* |
| AntT ID: | 538 | | $Na_2O$ | MgO | $Al_2O_3$ | $SiO_2$ | $P_2O_5$ | $K_2O$ | CaO | $TiO_2$ | MnO | FeO |
| Depth (m) | 50.41-50.50 | | 8.49 | 0.78 | 16.8 | 66.9 | 0.43 | 3.23 | 1.15 | 0.26 | 0.05 | 1.9 |
| Age (CE) | 1670-1671 | | 2.58 | 0.04 | 12.9 | 77.06 | 0.41 | 4.93 | 0.83 | 0.1 | 0 | 1.16 |
| Target Event: | N/A | *avg.* | *5.54* | *0.41* | *14.85* | *71.98* | *0.42* | *4.08* | *0.99* | *0.18* | *0.03* | *1.53* |
| | | *stdev.* | *4.18* | *0.52* | *2.76* | *7.18* | *0.01* | *1.20* | *0.23* | *0.11* | *0.04* | *0.52* |

**Table B.1**. Continued.

| AntT ID: | 545 | | $Na_2O$ | MgO | $Al_2O_3$ | $SiO_2$ | $P_2O_5$ | $K_2O$ | CaO | $TiO_2$ | MnO | FeO |
|---|---|---|---|---|---|---|---|---|---|---|---|---|
| Depth (m) | 58.00-58.12 | | 3.38 | 1.22 | 11.68 | 75.57 | 0.36 | 4.17 | 1.3 | 0.31 | 0.06 | 1.94 |
| Age (CE) | 1600 | | 5 | 0.23 | 13.69 | 74.29 | 1.48 | 3.33 | 1.12 | 0 | 0 | 0.87 |
| Target Event: | Huaynaputina | | 3.7 | 0.83 | 13.86 | 72.12 | 1.1 | 3.2 | 1.82 | 0.84 | 0.24 | 2.28 |
| | | | 5.48 | 0.89 | 11.48 | 74.56 | 0.93 | 3.15 | 0.75 | 0.4 | 0.22 | 2.15 |
| | | | 6.23 | 0.26 | 16.24 | 68.32 | 1.27 | 2.88 | 1.42 | 0.61 | 0.17 | 2.6 |
| | | | 4.36 | 0.27 | 13.28 | 72.04 | 0.72 | 3.61 | 1.73 | 0.82 | 0.2 | 2.97 |
| | | | 5.81 | 0.75 | 14.68 | 69.53 | 0.23 | 3.63 | 2.25 | 0.39 | 0.17 | 2.58 |
| | | | 3.77 | 0.21 | 11.58 | 73.59 | 1.71 | 3.94 | 2.11 | 0.58 | 0.18 | 2.32 |
| | | | 3.36 | 0.56 | 11.44 | 74.5 | 0.8 | 4.04 | 1.72 | 0.62 | 0.3 | 2.66 |
| | | | 3.57 | 0.65 | 12.38 | 74.39 | 0.67 | 3.84 | 1.3 | 0.45 | 0.19 | 2.55 |
| | | *avg.* | *4.47* | *0.59* | *13.03* | *72.89* | *0.93* | *3.58* | *1.55* | *0.50* | *0.17* | *2.29* |
| | | *stdev.* | *1.08* | *0.34* | *1.62* | *2.37* | *0.47* | *0.43* | *0.46* | *0.25* | *0.09* | *0.58* |
| AntT ID: | 546 | | $Na_2O$ | MgO | $Al_2O_3$ | $SiO_2$ | $P_2O_5$ | $K_2O$ | CaO | $TiO_2$ | MnO | FeO |
| Depth (m) | 58.12-58.23 | | 2.54 | 5.17 | 11.03 | 69.05 | 2.08 | 3.54 | 1.08 | 0.36 | 0.22 | 4.92 |
| Age (CE) | 1598-1600 | | | | | | | | | | | |
| Target Event: | Huaynaputina | | | | | | | | | | | |
| AntT ID: | 549 | | $Na_2O$ | MgO | $Al_2O_3$ | $SiO_2$ | $P_2O_5$ | $K_2O$ | CaO | $TiO_2$ | MnO | FeO |
| Depth (m) | 58.40-58.46 | | 4.63 | 3.24 | 14.74 | 55.18 | 1 | 2.73 | 5.66 | 0.92 | 0.23 | 11.65 |
| Age (CE) | 1596 | | 7.96 | 0.64 | 17.23 | 62.76 | 1.07 | 5.08 | 3.27 | 0.08 | 0.12 | 1.8 |
| Target Event: | Nevado del Ruiz | | 7.42 | 0.52 | 17.76 | 62.11 | 0.63 | 2.21 | 4.39 | 2.38 | 0.13 | 2.45 |
| | | | 6.2 | 1.63 | 12.37 | 61.5 | 0.49 | 4.77 | 3.61 | 1.31 | 0.21 | 7.91 |
| | | | 9.43 | 1.48 | 19.84 | 58.71 | 0.71 | 2.19 | 4.28 | 0.07 | 0.09 | 3.2 |
| | | | 4.31 | 2.17 | 12.84 | 56.43 | 1.2 | 2.08 | 6.64 | 1.12 | 0.19 | 13.02 |
| | | *avg.* | *6.66* | *1.61* | *15.80* | *59.45* | *0.85* | *3.18* | *4.64* | *0.98* | *0.16* | *6.67* |
| | | *stdev.* | *1.99* | *1.01* | *2.96* | *3.17* | *0.28* | *1.38* | *1.28* | *0.86* | *0.06* | *4.90* |

**Table B.1**. Continued.

| AntT ID: | 552 | | $Na_2O$ | MgO | $Al_2O_3$ | $SiO_2$ | $P_2O_5$ | $K_2O$ | CaO | $TiO_2$ | MnO | FeO |
|---|---|---|---|---|---|---|---|---|---|---|---|---|
| Depth (m) | 58.64-58.69 | | 4.73 | 0.07 | 19.07 | 65.5 | 0.49 | 7.43 | 1.07 | 0.16 | 0.04 | 1.43 |
| Age (CE) | 1594-1595 | | 7.3 | 0.4 | 19.19 | 58.7 | 0.82 | 1.72 | 1.66 | 0.75 | 0.05 | 9.41 |
| Target Event: | Nevado del Ruiz | | 8.77 | 0.55 | 18.53 | 52.68 | 0.91 | 7.23 | 1.48 | 0.67 | 0.04 | 9.14 |
| | | *avg.* | *6.93* | *0.34* | *18.93* | *58.96* | *0.74* | *5.46* | *1.40* | *0.53* | *0.04* | *6.66* |
| | | *stdev.* | *2.04* | *0.25* | *0.35* | *6.41* | *0.22* | *3.24* | *0.30* | *0.32* | *0.01* | *4.53* |
| AntT ID: | 553 | | $Na_2O$ | MgO | $Al_2O_3$ | $SiO_2$ | $P_2O_5$ | $K_2O$ | CaO | $TiO_2$ | MnO | FeO |
| Depth (m) | 58.69-58.79 | | 3.63 | 0.09 | 14.64 | 72.49 | 0 | 6.17 | 0.96 | 0.26 | 0.02 | 1.72 |
| Age (CE) | 1593-1594 | | 3.3 | 0 | 14.12 | 72.91 | 0.63 | 6.04 | 0.79 | 0.27 | 0.06 | 1.88 |
| Target Event: | Nevado del Ruiz | | 3.25 | 0.34 | 15.92 | 69.61 | 0 | 8.25 | 0.87 | 0.31 | 0.05 | 1.41 |
| | Billy Mitchell | | 4.75 | 0.46 | 12.73 | 69.42 | 1.72 | 3.09 | 1.97 | 0.1 | 0.04 | 5.72 |
| | | | 5 | 0.46 | 14.49 | 62.65 | 2.08 | 4.03 | 3.33 | 0.66 | 0.1 | 7.2 |
| | | *avg.* | *3.99* | *0.27* | *14.38* | *69.42* | *0.89* | *5.52* | *1.58* | *0.32* | *0.05* | *3.59* |
| | | *stdev.* | *0.83* | *0.21* | *1.14* | *4.11* | *0.97* | *2.02* | *1.09* | *0.21* | *0.03* | *2.68* |
| AntT ID: | 560 | | $Na_2O$ | MgO | $Al_2O_3$ | $SiO_2$ | $P_2O_5$ | $K_2O$ | CaO | $TiO_2$ | MnO | FeO |
| Depth (m) | 91.88-92.00 | | 5.77 | 1.83 | 14.62 | 66 | 0.12 | 3.86 | 3.91 | 1.07 | 0.16 | 2.66 |
| Age (CE) | 1256-1257 | | | | | | | | | | | |
| Target Event: | Samalas | | | | | | | | | | | |
| AntT ID: | 612 | | $Na_2O$ | MgO | $Al_2O_3$ | $SiO_2$ | $P_2O_5$ | $K_2O$ | CaO | $TiO_2$ | MnO | FeO |
| Depth (m) | 438.06-438.10 | | 5.74 | 0.87 | 13.65 | 61.41 | 0 | 1.28 | 4.52 | 0.98 | 0.08 | 11.49 |
| Age (CE) | 3516 BCE | | 9.26 | 0.75 | 13.43 | 61.13 | 0.51 | 2.83 | 1.19 | 0.65 | 0.64 | 9.62 |
| Target Event: | Pinatubo/Tarawera | | 7.41 | 0.83 | 13.13 | 60.37 | 0.32 | 1.57 | 4.23 | 0.71 | 0.23 | 11.19 |
| | | *avg.* | *7.47* | *0.82* | *13.40* | *60.97* | *0.28* | *1.89* | *3.31* | *0.78* | *0.32* | *10.77* |
| | | *stdev.* | *1.76* | *0.06* | *0.26* | *0.54* | *0.26* | *0.82* | *1.84* | *0.18* | *0.29* | *1.00* |

**Table B.1**. Continued.

| AntT ID: | 613 | | $Na_2O$ | MgO | $Al_2O_3$ | $SiO_2$ | $P_2O_5$ | $K_2O$ | CaO | $TiO_2$ | MnO | FeO |
|---|---|---|---|---|---|---|---|---|---|---|---|---|
| Depth (m) | 438.10-438.14 | | 6.13 | 0.11 | 15.52 | 62.78 | 2.66 | 9.09 | 1.18 | 0.43 | 0.29 | 1.8 |
| Age (CE) | 3517 BCE | | | | | | | | | | | |
| Target Event: | Pinatubo/Tarawera | | | | | | | | | | | |
| AntT ID: | 614 | | $Na_2O$ | MgO | $Al_2O_3$ | $SiO_2$ | $P_2O_5$ | $K_2O$ | CaO | $TiO_2$ | MnO | FeO |
| Depth (m) | 438.14-438.19 | | 3.98 | 0.69 | 11.92 | 65.92 | 1.83 | 1.9 | 2.32 | 1.37 | 0.18 | 9.89 |
| Age (CE) | 3518 BCE | | 2.37 | 0.4 | 13.57 | 67.58 | 1.31 | 1.06 | 2.54 | 1.07 | 0.4 | 9.7 |
| Target Event: | Pinatubo/Tarawera | | 5.51 | 0.3 | 13.27 | 67.42 | 0.28 | 1.17 | 2.71 | 1.01 | 0.15 | 8.18 |
| | | | 6.3 | 0.41 | 11.35 | 64.53 | 0.26 | 1.48 | 3.99 | 1.31 | 0.12 | 10.25 |
| | | | 4.71 | 0.37 | 12.91 | 63.27 | 1.2 | 1.11 | 3.8 | 0.88 | 0.19 | 11.56 |
| | | *avg.* | *4.57* | *0.43* | *12.60* | *65.74* | *0.98* | *1.34* | *3.07* | *1.13* | *0.21* | *9.92* |
| | | *stdev.* | *1.51* | *0.15* | *0.94* | *1.86* | *0.69* | *0.35* | *0.77* | *0.21* | *0.11* | *1.21* |
| AntT ID: | 627 | | $Na_2O$ | MgO | $Al_2O_3$ | $SiO_2$ | $P_2O_5$ | $K_2O$ | CaO | $TiO_2$ | MnO | FeO |
| Depth (m) | 511.30-511.37 | | 5.08 | 0.26 | 12.87 | 71.01 | 0.54 | 3.43 | 2.61 | 0.16 | 0.33 | 3.72 |
| Age (CE) | 4527-4525 BCE | | 4.84 | 0.13 | 13.35 | 73.13 | 0.51 | 2.9 | 1.23 | 0.11 | 0.42 | 3.39 |
| Target Event: | N/A | | 4.66 | 0.17 | 13.21 | 73.93 | 0.37 | 2.9 | 1.23 | 0.14 | 0.36 | 3.04 |
| | | | 4.51 | 0.19 | 13.32 | 72.49 | 1.04 | 2.67 | 1.39 | 0.18 | 0.14 | 4.08 |
| | | | 2.71 | 0.23 | 13.03 | 73.81 | 1.54 | 2.59 | 1.26 | 0.27 | 0.83 | 3.72 |
| | | | 3.5 | 0.25 | 13.49 | 73.12 | 0.42 | 2.89 | 1.07 | 0.15 | 0.71 | 4.39 |
| | | | 3.33 | 0.16 | 12.75 | 75.31 | 0.22 | 2.79 | 1.46 | 0.15 | 0.31 | 3.54 |
| | | | 4.43 | 0.16 | 12.94 | 75.15 | 0.23 | 2.59 | 1.18 | 0.17 | 0.38 | 2.76 |
| | | | 3.86 | 0.17 | 13.82 | 73.16 | 0.54 | 2.65 | 1.27 | 0.15 | 0.61 | 3.78 |
| | | | 4.95 | 0.13 | 13.04 | 73.03 | 0.33 | 2.95 | 1.54 | 0.21 | 0.6 | 3.21 |
| | | *avg.* | *4.19* | *0.19* | *13.18* | *73.41* | *0.57* | *2.84* | *1.42* | *0.17* | *0.47* | *3.56* |
| | | *stdev.* | *0.79* | *0.05* | *0.32* | *1.25* | *0.41* | *0.25* | *0.44* | *0.04* | *0.21* | *0.49* |

**Table B.1**. Continued.

| AntT ID: | 619 | | $Na_2O$ | MgO | $Al_2O_3$ | $SiO_2$ | $P_2O_5$ | $K_2O$ | CaO | $TiO_2$ | MnO | FeO |
|---|---|---|---|---|---|---|---|---|---|---|---|---|
| Depth (m) | 711.27-711.34 | | 2.23 | 1.67 | 16.38 | 65.14 | 0.55 | 3.54 | 1.2 | 0.4 | 1.59 | 7.3 |
| Age (CE) | 7838-7837 BCE | | | | | | | | | | | |
| Target Event: | Chaitén | | | | | | | | | | | |
| AntT ID: | 600 | | $Na_2O$ | MgO | $Al_2O_3$ | $SiO_2$ | $P_2O_5$ | $K_2O$ | CaO | $TiO_2$ | MnO | FeO |
| Depth (m) | 726.38-726.49 | | 6.28 | 0.24 | 14.03 | 72.33 | 0.38 | 2.37 | 1.14 | 0.19 | 0.33 | 2.71 |
| Age (CE) | 8128-8126 BCE | | 5 | 0.51 | 13.63 | 71.03 | 1.16 | 1.79 | 1.53 | 0.31 | 0.78 | 4.27 |
| Target Event: | Taupo | | 5.69 | 0.3 | 13.9 | 70.95 | 1.13 | 2.27 | 1.3 | 0.29 | 0.62 | 3.55 |
| | | | 3 | 0.13 | 12.47 | 73.86 | 1.86 | 1.88 | 1.47 | 0.41 | 0.54 | 4.38 |
| | | | 4.53 | 0.19 | 13.37 | 72.4 | 0.35 | 2.73 | 1.52 | 0.44 | 0.93 | 3.53 |
| | | | 4.86 | 0.3 | 14.5 | 70.28 | 0.27 | 2.26 | 1.64 | 0.39 | 0.85 | 4.64 |
| | | *avg.* | *4.89* | *0.28* | *13.65* | *71.81* | *0.86* | *2.22* | *1.43* | *0.34* | *0.68* | *3.85* |
| | | *stdev.* | *1.12* | *0.13* | *0.69* | *1.30* | *0.63* | *0.34* | *0.18* | *0.09* | *0.22* | *0.72* |
| AntT ID: | 601 | | $Na_2O$ | MgO | $Al_2O_3$ | $SiO_2$ | $P_2O_5$ | $K_2O$ | CaO | $TiO_2$ | MnO | FeO |
| Depth (m) | 726.49-726.57 | | 5.32 | 0.45 | 15.33 | 69.26 | 0.22 | 1.95 | 2.49 | 0.28 | 0.41 | 4.27 |
| Age (CE) | 8130-8128 BCE | | | | | | | | | | | |
| Target Event: | Taupo | | | | | | | | | | | |
| AntT ID: | 603 | | $Na_2O$ | MgO | $Al_2O_3$ | $SiO_2$ | $P_2O_5$ | $K_2O$ | CaO | $TiO_2$ | MnO | FeO |
| Depth (m) | 726.61-726.72 | | 7.33 | 1.96 | 15.7 | 62.33 | 0.47 | 6.81 | 0.35 | 0.16 | 0.5 | 4.39 |
| Age (CE) | 8133-8131 BCE | | 4.94 | 0.07 | 12.81 | 75.73 | 0.21 | 4.82 | 0.24 | 0.04 | 0.32 | 0.82 |
| Target Event: | Taupo | | 3.38 | 0.13 | 12.86 | 75.61 | 0.65 | 4.29 | 0.4 | 0.31 | 0.93 | 1.43 |
| | | *avg.* | *5.22* | *0.72* | *13.79* | *71.22* | *0.44* | *5.31* | *0.33* | *0.17* | *0.58* | *2.21* |
| | | *stdev.* | *1.99* | *1.07* | *1.65* | *7.70* | *0.22* | *1.33* | *0.08* | *0.14* | *0.31* | *1.91* |
| AntT ID: | 604 | | $Na_2O$ | MgO | $Al_2O_3$ | $SiO_2$ | $P_2O_5$ | $K_2O$ | CaO | $TiO_2$ | MnO | FeO |
| Depth (m) | 726.72-726.79 | | 7.74 | 0.64 | 12.19 | 63.54 | 1.67 | 4.69 | 0.87 | 0.49 | 0.79 | 7.38 |
| Age (CE) | 8135-8133 BCE | | | | | | | | | | | |
| Target Event: | N/A | | | | | | | | | | | |

**Table B.1**. Continued.

| AntT ID: | 636 | | $Na_2O$ | MgO | $Al_2O_3$ | $SiO_2$ | $P_2O_5$ | $K_2O$ | CaO | $TiO_2$ | MnO | FeO |
|---|---|---|---|---|---|---|---|---|---|---|---|---|
| Depth (m) | 784.12-784.22 | | 5.54 | 0.84 | 15.63 | 68.68 | 0.41 | 3.26 | 2.1 | 0.21 | 0.34 | 2.99 |
| Age (CE) | 9150-9148 BCE | | 6.89 | 1.31 | 16.61 | 61.5 | 0.29 | 2.53 | 3.89 | 0.18 | 0.57 | 6.23 |
| Target Event: | N/A | | 5.88 | 0.2 | 12.09 | 74.5 | 0.23 | 4.22 | 0.91 | 0.12 | 0.45 | 1.4 |
| | | | 5 | 0.18 | 12.35 | 76.05 | 0.12 | 4.31 | 0.9 | 0.13 | 0.14 | 0.82 |
| | | | 3.78 | 0.2 | 10.76 | 76.43 | 0.44 | 4.73 | 0.38 | 0.23 | 1.41 | 1.65 |
| | | | 8.14 | 0.82 | 15.78 | 61.76 | 1.13 | 3.38 | 3 | 0.3 | 0.62 | 5.06 |
| | | *avg.* | *5.87* | *0.59* | *13.87* | *69.82* | *0.44* | *3.74* | *1.86* | *0.20* | *0.59* | *3.03* |
| | | *stdev.* | *1.51* | *0.47* | *2.43* | *6.93* | *0.36* | *0.82* | *1.38* | *0.07* | *0.44* | *2.18* |
| AntT ID: | 596 | | $Na_2O$ | MgO | $Al_2O_3$ | $SiO_2$ | $P_2O_5$ | $K_2O$ | CaO | $TiO_2$ | MnO | FeO |
| Depth (m) | 785.95-786.00 | | 5.25 | 2.35 | 13.51 | 68.86 | 0.13 | 3.13 | 3.08 | 1.21 | 0 | 2.49 |
| Age (CE) | 9180-9179 BCE | | 7.87 | 0.32 | 18.34 | 65.05 | 0.01 | 6.4 | 1.43 | 0.28 | 0.03 | 0.27 |
| Target Event: | Taupo | | 4.28 | 0.49 | 12.13 | 75.39 | 0.17 | 5.07 | 1.23 | 0.43 | 0.16 | 0.65 |
| | | | 2.68 | 0.49 | 11.74 | 76 | 0.17 | 5.51 | 1.69 | 0.82 | 0.24 | 0.66 |
| | | *avg.* | *5.02* | *0.91* | *13.93* | *71.33* | *0.12* | *5.03* | *1.86* | *0.69* | *0.11* | *1.02* |
| | | *stdev.* | *2.18* | *0.96* | *3.04* | *5.29* | *0.08* | *1.38* | *0.84* | *0.42* | *0.11* | *1.00* |
| AntT ID: | 597 | | $Na_2O$ | MgO | $Al_2O_3$ | $SiO_2$ | $P_2O_5$ | $K_2O$ | CaO | $TiO_2$ | MnO | FeO |
| Depth (m) | 786.00-786.05 | | 3.33 | 1.31 | 13.83 | 73.25 | 0.12 | 3.21 | 2.15 | 0.59 | 0.07 | 2.14 |
| Age (CE) | 9181-9180 BCE | | 4.86 | 1.02 | 13.11 | 72.43 | 0.15 | 2.61 | 2.57 | 0.54 | 0.09 | 2.6 |
| Target Event: | Taupo | | 2.85 | 7.66 | 15.76 | 63.66 | 0.08 | 2.97 | 1.57 | 0.81 | 0 | 4.63 |
| | | *avg.* | *3.68* | *3.33* | *14.23* | *69.78* | *0.12* | *2.93* | *2.10* | *0.65* | *0.05* | *3.12* |
| | | *stdev.* | *1.05* | *3.75* | *1.37* | *5.32* | *0.04* | *0.30* | *0.50* | *0.14* | *0.05* | *1.32* |

**Table B.1**. Continued.

| AntT ID: | 581 | | $Na_2O$ | MgO | $Al_2O_3$ | $SiO_2$ | $P_2O_5$ | $K_2O$ | CaO | $TiO_2$ | MnO | FeO |
|---|---|---|---|---|---|---|---|---|---|---|---|---|
| Depth (m) | 787.83-787.89 | | 3.62 | 0.52 | 12.12 | 78.16 | 0.1 | 4.01 | 0.77 | 0.3 | 0.04 | 0.37 |
| Age (CE) | 9214-9213 BCE | | 3.43 | 0.33 | 12.1 | 78.27 | 0.05 | 4.18 | 0.98 | 0.23 | 0.06 | 0.37 |
| Target Event: | Taupo | | 2.13 | 0.64 | 12.58 | 78.59 | 0.27 | 3.82 | 0.88 | 0.23 | 0.1 | 0.78 |
| | | | 2.79 | 0.61 | 12.93 | 77.36 | 0.31 | 4.73 | 0.57 | 0 | 0.11 | 0.58 |
| | | | 2.88 | 0.31 | 12.47 | 76.53 | 0.13 | 5.93 | 1.01 | 0.26 | 0.04 | 0.44 |
| | | | 2.15 | 0.44 | 12.53 | 77.54 | 0.03 | 5.76 | 0.93 | 0.19 | 0.03 | 0.4 |
| | | | 4.28 | 0.64 | 13.58 | 74.02 | 0.04 | 4.66 | 1.56 | 0.39 | 0.08 | 0.75 |
| | | | 2.69 | 0.53 | 11.9 | 79.74 | 0.04 | 3.36 | 0.92 | 0.26 | 0.08 | 0.46 |
| | | | 2.58 | 0.67 | 11.44 | 79.61 | 0.06 | 4.54 | 0.42 | 0.13 | 0.03 | 0.52 |
| | | *avg.* | *2.95* | *0.52* | *12.41* | *77.76* | *0.11* | *4.55* | *0.89* | *0.22* | *0.06* | *0.52* |
| | | *stdev.* | *0.71* | *0.14* | *0.62* | *1.74* | *0.11* | *0.85* | *0.32* | *0.11* | *0.03* | *0.16* |
| AntT ID: | 582 | | $Na_2O$ | MgO | $Al_2O_3$ | $SiO_2$ | $P_2O_5$ | $K_2O$ | CaO | $TiO_2$ | MnO | FeO |
| Depth (m) | 787.89-787.93 | | 2.81 | 0.87 | 12.04 | 76.28 | 0.11 | 5.15 | 1.11 | 0.4 | 0.2 | 1.04 |
| Age (CE) | 9215 BCE | | 3.11 | 0.42 | 13.12 | 73.52 | 0.13 | 7.73 | 0.88 | 0.43 | 0.13 | 0.53 |
| Target Event: | Taupo | | 3.16 | 0.71 | 12.89 | 75.95 | 0 | 5.43 | 1.12 | 0.05 | 0.1 | 0.59 |
| | | *avg.* | *3.03* | *0.67* | *12.68* | *75.25* | *0.08* | *6.10* | *1.04* | *0.29* | *0.14* | *0.72* |
| | | *stdev.* | *0.19* | *0.23* | *0.57* | *1.51* | *0.07* | *1.42* | *0.14* | *0.21* | *0.05* | *0.28* |

*Note: Analytical precision, based on replicate analyses of rhyolitic and basaltic reference material, are as follows (all in wt.%):*
*Rhyolite: $Na_2O$±1.39, MgO± 0.09, $Al_2O_3$± 0.57, $SiO_2$±1.40, $P_2O_5$±0.11, $K_2O$±0.82, CaO±0.53, $TiO_2$±0.71, MnO±0.43, FeO±1.19.*
*Basalt: $Na_2O$±0.98, MgO± 3.77, $Al_2O_3$± 0.61, $SiO_2$±2.16, $P_2O_5$±0.17, $K_2O$±0.07, CaO±1.86, $TiO_2$±0.52, MnO±0.25, FeO±3.75.*

**Table B.2.** SEM-EDS operating conditions

| | |
|---|---|
| **Method** | UMaine Tephra SEM-EDS 20210520 |
| **Technique** | SEM-EDS |
| **Instrument** | Tescan Vega II XMU |
| **Detector** | Apollo40 SSD |
| **Lab Information** | Electron Microscopy Laboratory, The University of Maine, https://umaine.edu/earthclimate/facilities/electron-microscopy-laboratory/ |
| **Beam Conditions** | 15 kV, 140 nA, focused beam |
| **Acquisition Time (seconds)** | 100 (for session conditions for AntT 483, see Table A.2.) |
| **Secondary Reference Materials** | Varies |
| **EDS Utilized?** | Yes |
| **EDS Software** | EDAX Genesis v6.1 |
| **Oxide Calculation Procedure** | EDAX Genesis v6.1 PhiRhoZ and USNM 72854 VG-568 rhyolitic glass standard |
| **EDS PC OS** | Windows XP |

## APPENDIX C: UNABRIDGED METHODOLOGY

### C.1. Sample Processing and Freezer Sampling

All stages of ice core sample processing are conducted under clean room conditions using clean ice handling and processing protocols. A temperature of -20 ℃ is maintained inside of a HEPA filtered air clean room environment. Here, ice core sections (typically 1 meter in length) are measured, sectioned, decontaminated, and packaged according to the desired sampling plan or protocol.

#### C.1.1. Supplies and Materials:

- High-Density Polyethylene Plastic (HDPE) cutting board
- Stainless steel tongs
- 0.7 L Whirl-Pak® bags
- Meter stick and centimeter ruler
- Methanol
- Scalpel handle and stainless blades
- Ceramic knife
- Kimwipes®
- Coping saw
- Sterile Gloves
- Cooler

#### C.1.2. Cold Room Workflow:

1. To prevent contamination all items to be used in sample processing, including the in-freezer clean room bench-top, are precleaned.
    a. HDPA cutting board and utensils (knifes, saws, tongs, and blades) are rinsed in deionized water prior to entering the cold room.
    b. Cold room bench top, meter stick, and centimeter ruler are cleaned with methanol and kimwipes prior to introducing the ice core sample to the cold room
2. Carefully transfer ice core samples from the shipping box (or other container) to the cold clean room.
3. Position the original ice core sample such that the ice core “top” (marked with arrow) faces right and the “bottom” faces left.

4. Determine and note the top reference depth of the original ice core sample, which is noted on the original packaging. Open the “top” end of the packaging and make all measurements from this end.
5. Carefully remove the original ice core sample from its packaging and place it onto a pre-cleaned cutting board.
6. Starting with the “top” end of the original ice core sample, measure down-depth (to the left) to the appropriate depth to meet your desired sampling resolution or targeted depth interval suspected to contain tephra (Figure C.1.A.).
7. Using a pre-cleaned coping saw, cut the original ice core at this measured depth. Pre-cleaned tongs may be used to secure the original ice core sample so that it is easier to cut.
8. Using a pre-cleaned blade or ceramic knife, shave the outermost layer (0.5 mm) of contaminated ice from all faces of the sectioned sample. Pre-cleaned tongs may be used to hold the sectioned sample in place whilst shaving, but for smaller sections it may be necessary to hold the sectioned sample with a sterile-gloved hand (Figure C.1.B).
9. Place the decontaminated sectioned sample into a 0.7 L Whirl-Pak bag or a pre-cleaned Nalgene container and label appropriately (Sample ID, top depth, bottom depth).
10. Repeat the above steps for each desired interval. It is necessary to clean and decontaminate all surfaces and utensils between intervals to prevent cross contamination.
11. After the freezer sampling session, place all prepared samples into a cooler for transport.

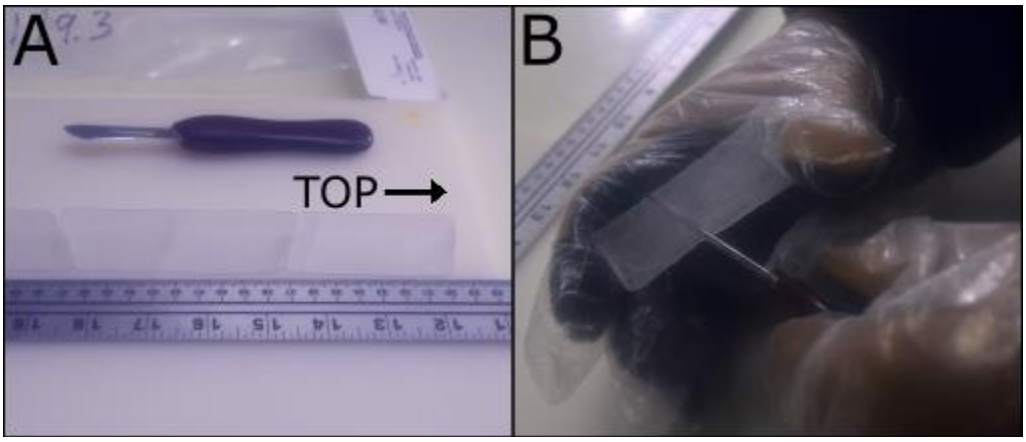


Figure C.1. Freezer Methods. (A) Orientation and measuring: place the ice core in the proper orientation, with the top depth on your right. (B) Decontamination: carefully shave all faces of the sectioned ice core sample with a pre-cleaned blade to remove any surface contaminants.

**C.2. Sample Processing: Tephra Separation and Sample Mounting**

All stages of ice core sample processing are conducted under clean room conditions using ice handling and processing protocols.

**C.2.1. Required Materials:**

- Heated water bath
- Falcon 15ml polypropylene conical (17 x 120 mm style) centrifuge vials
- Centrifuge
- Isopore ™ 0.2 µm polycarbonate micropore filters
- 10 - 100 µL pipette and tips
- 1.25” diameter Buehler ring mount
- Hard-drive disk platter
- 5 mill Single-Sided Polyamide Kapton Tape (K-Tape)
- Hot plate
- Buehler EpoThin 2 epoxy and mixing materials (cups, stirring sticks)

**C.2.2. Tephra Separation:**

1. To prevent contamination, all melting and mounting procedures should be conducted in a clean-room environment with new or sterile materials.
2. Rapidly melt samples by placing each 0.7 L Whirl-Pak bag containing a frozen, decontaminated, sectioned ice core sample into a hot water bath (40 °C).

3. Once melted, promptly remove the 0.7 L Whirl-Pak bag containing the now melted sample from the hot water bath.
4. Aliquot the sample meltwater into labeled (Sample ID) Falcon 15 mL polypropylene conical tube (17 x 120 mm style) centrifuge vials and transfer to the centrifuge. Ensure that the centrifuge rotor is balanced by placing centrifuge vials containing blanks in the rotor as necessary.
5. Centrifuge the vials at 5000 rpm for 10 minutes.

**C.2.3. Mounting Assemblage Preparation:**

1. Split a Buehler ring form in two by cutting perpendicular to the c-axis. Take care to mark the circular face which was cut.
2. Grind the non-cut (non-marked, original surface) face of each mount flat using 400-grit sandpaper.
3. Remove any cutting debris from the inside of the ring.
4. Rinse the ring in Milli-Q and clean in an ultrasonic bath for 3 minutes.
5. To ensure a flat mounting surface, obtain a computer hard drive disk or other similar ultra-flat metal surface.
6. Using denatured alcohol, clean the disk, ensuring the surface is scratch and residue-free. Repeat as necessary.
7. Cut a strip of 26 mm wide 5 mill Single-Sided Polyamide Kapton Tape (K-tape) and lay the tape on the disk with the adhesive facing upwards. Use more tape to fix the original strip to the disk (Figure C.2.)
8. Adhere non-cut circular face (original surface) of the ring form to the K-tape. The marked cut circular face should be exposed (Figure C.2.).
9. Test the seal of the ring form by squirting distilled water into the ring. If no water leaks from the edges, you have a satisfactory seal. If you have a leak, press to reseal the ring to the tape. If the seal is still unsatisfactory, you need to remove the tape and begin step 5 again.
10. Once the seal is cleared, place the hard drive assemblage on a hot plate (60-70 °C) until the water has completely evaporated.

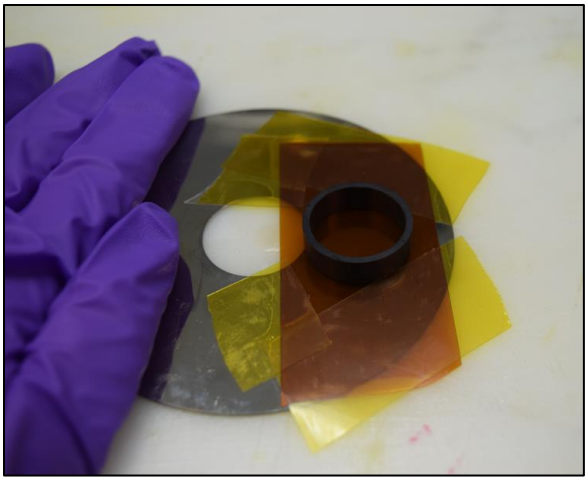

Figure C.2. Mounting Apparatus. A completed tephra mounting apparatus.

### C.2.4. Adding Sample and Finishing the Mount:

1. Leaving the assemblage on the hot plate, use a long-tipped pipette to remove 40 µL from the bottom of each vial and drop into the center of the ring mount (Figure C.3.).

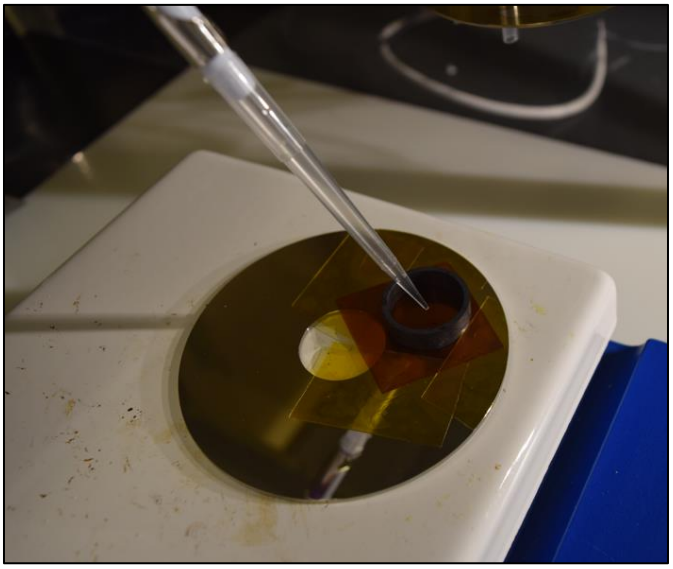

Figure C.3. Addition of Sample. 40 microliters of ice core sample meltwater being pipetted to the center of a ring mount and tephra mounting apparatus.

2. Allow the water from the previous vial to evaporate completely before adding more sample.

3. It is imperative that only a small amount of sample meltwater (0.40 microliters) be added to the hot plate at a time to reduce the possibility of sample spreading and potential loss from contact with the ring mount edges.
4. When finished evaporating from each vial, filter the remaining water through a 0.2 µm polycarbonate micropore filter. Place filters in covered petri dishes under the hood to dry.
5. When water has finished evaporating, remove the mounting assemblage from the hot plate and allow to cool.
6. Mix Buehler EpoThin 2 epoxy according to manufacturer's instructions.
7. Once mixed, degas the epoxy by placing the vessel containing the epoxy into a pressure chamber and pump down the vacuum to -30 in Hg for 30 seconds.
8. Backfill ring mount(s) to the top and cure overnight (12 hours) (Figure C. 4.)

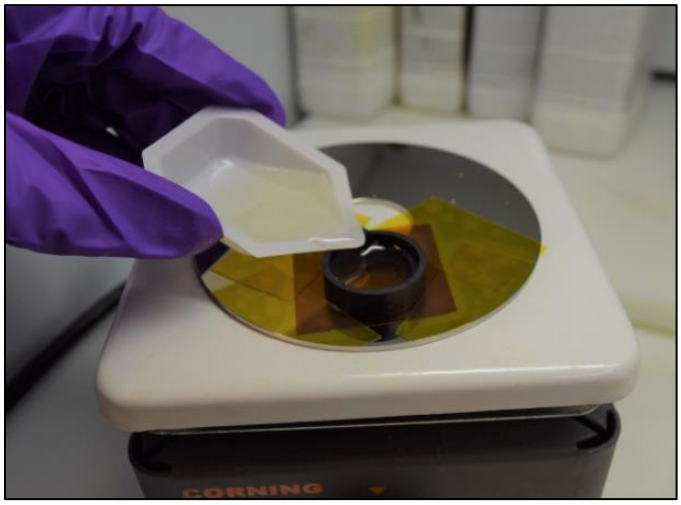


Figure C.4. Addition of Epoxy. The backfilling of a prepared sample with Buehler EpoThin 2 epoxy.

9. Once the epoxy has cured completely, gently lift the K-tape away from the hard drive disk.
10. Gently and slowly peel the ring mount away from the K-tape.

**C.3. SEM-EDS Tephra Analysis, Reconnaissance, and Imaging**

**C.3.1. Required Equipment (or equivalent):**

- Carbon coater
- Tescan Vega XMU scanning electron microscope (SEM)
- 40 mm2 EDAX ApolloTM energy dispersive x-ray detector (EDS)
- EDAX GenesisTM software

**C.3.2. Instrument and Software Setup:**

1. Samples can either be epoxy mounted tephra (see above instructions) or filter captured tephra (used primarily for pilot studies; follow only "Tephra Separation" steps 1-3 and "Adding Sample and Finishing the Mount" step 4). Note: if you plan to use filter captured tephra, you need a special sample holder (Figure 3).
2. Carbon coat all samples and standards.
3. Set the SEM to the following settings:
    a. Accelerating Voltage = 15 kV
    b. Tilt = 0°
    c. Probe Current = ~120-160 pA at PC 10 (PC settings may vary across instruments)
    d. Working Distance = 15 mm
    e. Electron Beam = ON
    f. Backscattered Electron (BSE) Detector = IN
4. Set the EDAX GenesisTM software settings to:
    a. Analyzer = EDS1
    b. Preset = 100 seconds of live time
    c. Amp Time = 12.8 µS
    d. Analysis = Standardless
5. All analyses are performed with a standardless analysis option, which necessitates normalizing the results to 100%.
6. Net peak intensities are converted to oxide weight percent using a standardless PhiRhoZ based correction (Packwood & Brown, 1981).
7. Each analysis accumulates the x-ray spectra over a single analytical spot.
8. Detection limits for all oxides are around 0.2 %.

### C.3.3. Secondary Standard Correction:

1. At the beginning of a session, navigate to a suitable secondary standard to apply an EDAX GenesisTM correction. The standard should be matrix matched, meaning if you are analyzing a rhyolitic eruption, your secondary standard should be rhyolitic in composition as well (e.g., Basaltic Glass NMNH 113498-1, Rhyolitic Glass NMNH 72854 VG-568).
2. Navigate to secondary standard.
3. With the working distance set to 15, focus on the grain. The Z should end up between 3 - 5, depending on your mount and holder.
4. Select the area of the grain to collect the spot analysis.
    a. Make sure that the area is homogeneous and free of surficial deformation.
    b. Set the collection area to be a 1 by 1 μm area.
5. Click “Collect” EDAX GenesisTM software to collect a spectra analysis of the secondary standard.
6. Once the analysis is finished, in the EDAX GenesisTM software:
    a. Press the two arrows in EXpretID section.
    b. Add standard elements to the PeakID list for the published values. To add an element to the list, type “ELEMENT” K (ex: for “Fe”, type “Fe K”). Element labels will appear on your spectra screen after you click enter.
    c. Press the two arrows in the Quant section.
    d. Click “Stds” button.
    e. Select “Compound” in the pop-up window. Then click “Setup” and select “Oxides”.
    f. Input standard values into the box for each compound.
    g. Click “RZAF”. Then select “Use as Compound” and press “Ok”.
    h. Click “SEC”. Then select “Update SEC Table” and press “Ok”.
    i. Press “Ok” in the pop-up window.
    j. Save as a .sec file to apply the analysis as a correction.

k. Next to the “Quant” button, right click and make sure that “SEC” is set to “User” and “Type” is set to “Oxides”.
l. To save the results as a viewable PDF, click “Quant” - “Print Results” - “Ok” - [Navigate to folder] - [Rename as necessary].

7. Analytical accuracy is tested by acquiring a spot analysis on one to two other secondary standards of known composition (e.g., BHVO-2G, ATHO-G, Lipari Obsidian) at the beginning and end of each session. This allows accuracy and instrument drift to be monitored.
    a. Navigate to secondary standard.
    b. Select the area of the grain to collect the spot analysis.
        i. Make sure that the area is homogeneous and free of surficial deformation.
        ii. Set the collection area to be a 1 by 1 µm area.
    c. Click “Collect” EDAX GenesisTM software to collect a spectra analysis of the secondary standard.
    d. Save as a .std file so that the file can be reopened with the EDAX GenesisTM software at a later date if necessary.
    e. To save the results as a viewable PDF, click “Quant” - “Print Results” - “Ok” - [Navigate to folder] - [Rename as necessary].

**C.3.4. Spot Analysis of Unknown Tephra**

1. Navigate to the sample mount and locate a grain.
2. Select the area of the grain to collect the spot analysis.
    a. Make sure that the area is homogeneous and free of surficial deformation.
    b. Set the collection area to be a 1 by 1 µm area.
3. Click “Collect” EDAX GenesisTM software to collect a spectra analysis of the secondary standard.
4. Make sure that the Peak ID list represents a useful suite of elements for tephra ID, using previously published values as a guide.
    a. A typical Peak ID list is: Si K, Ti K, AL K, Fe K, Mn K, Mg K, Ca K, Na K, K K, P K

b. To add an element to the list, type “ELEMENT” K (ex: for “Fe”, type “Fe K”). Element labels will appear on your spectra screen after you click enter.

5. Save as a .std file so that the file can be reopened with the EDAX GenesisTM software at a later date if necessary.
6. To save the results as a viewable PDF, click “Quant” - “Print Results” - “Ok” - [Navigate to folder] - [Rename as necessary].
7. Image the grain if desired.

**C.3.5. Imaging:**

1. Pull out the Backscattered Electron (BSE) Beam and switch to the Secondary Electron (SE) Beam.
2. Zoom in or out until the grain fills the frame.
3. Focus repeatedly with increasingly slower scan speeds.
4. Change the PC to 13.
5. Adjust the white and black values of the image.
    a. Click “Auto Signal”.
    b. Change the amplification and contrast as needed to manually adjust the image quality.
    c. Under “Panels”, open the “Histogram” panel to examine the balance of the image
6. Under “Setup”, select “Image Parameters” and set the desired output image quality (typically 4:3, 1024 x 728). Then change the save speed to 6 or 7 for a typical image capture.
7. Click “Acquire Image” on the right-side panel.
8. If the image is shaky, open the air bottle. This will suspend the entire SEM and reduce environmental vibrations. Allow the SEM to stabilize before reacquiring the image, and remember to close the air bottle when finished.
9. Once the image is acquired, a pop-up window will appear prompting the user to save the file. To save the results, [Navigate to folder] - [Rename as necessary].

### C.4. EPMA-WDS Tephra Analysis

#### C.4.1. Required Equipment (or equivalent):

- Carbon coater
- Cameca SX-100

#### C.4.2. Instrument and Software Setup:

1. Polish the mount before microprobe analysis following Iverson et al. (2017).
2. Set the spectrometers to the following crystal orientations:
    a. Spectrometer 1 = thallium acid phthalate (TAP) crystal
    b. Spectrometer 2 = large area pentaerythritol (LPET) crystal
    c. Spectrometer 3 = large area lithium fluorite (LLiF) crystal
    d. Spectrometer 4 = large area thallium acid phthalate (LTAP) crystal
    e. Spectrometer 5 = large area pentaerythritol (LPET) crystal
3. Set the microprobe for tephra analysis following the method developed by Hayward (2012). Use three different analytical conditions to prevent Na migration, optimize precision, and maximize detection limits of minor elements:
    a. NaKα and AlKα were analyzed on a TAP crystal at 15 kV, 0.5 nA, a 6 µm beam
    b. SiKα(TAP), CaKα(2 PET), KKα(2 PET), MgKα(TAP) and FeKα(LiF) were analyzed at 15 kV, 2 nA, and a 6 µm beam
    c. FKα(2 TAP), PKα(2 PET), SKα(2 PET), ClKα(2 PET), TiKα(2 PET), and FeKα(LiF) were analyzed at 15 kV, 80 nA, and a 6 µm beam
4. Use the simple silicate and oxide standards and the matrix correction of Merlet (1994).
5. Counting times varied from 20 to 80 sec.
6. Analyze Smithsonian Rhyolite Glass (NMNH 72854 VG-568) and Smithsonian Basaltic Glass (NMNH 113498-I (A99)) before and after each analytical session as reference materials to monitor analytical accuracy and precision.

7. Both the tephra and standards were analyzed under identical conditions, using the following standards and instrument parameters:
    a. Jadeite (NaKα, 20 sec on LTAP)
    b. Sanidine (AlKα, 20 sec on TAP; SiKα, 20 sec on TAP; KKα, 20 sec on 2 LPET)
    c. Wollastonite (CaKα, 20 sec on 2 LPET)
    d. Spinel (MgKα, 40 sec on LTAP)
    e. Magnetite (FeKα, 40 sec on LLiF)
    f. Polylithionite (FKα, 80 sec on TAP)
    g. Tugtupite (ClKα, 20 sec on 2 LPET)
    h. Barite (SKα, 20 sec on 2 PET)
    i. Apatite (PKα, 20 sec on 2 LPET)
    j. Rutile (TiKα, 20 sec on 2 LPET)
    k. Rhodonite (MnKα, 80 sec on LLiF)

## APPENDIX D: ANIAKCHAK TEPHRA IN THE GISP2 ICE CORE

The following data is the University of Maine's contribution to a collaborative paper (Pearson et al., 2022) published in PNAS Nexxus.

**Table D.1.** GISP2 Glass Geochemistry (774.53-774.78 m depth), SEM-EDS. Geochemical data is calculated using EDAX Genesis quantification procedure with NMNH 72854 Rhyolite Glass standard. All data were collected under SEM-EDS operating conditions found in Table B.2. All measurements are in weight percent oxide and are normalized to 100% weight percent. "n" represents the total number of analyses. Analytical accuracy and precision, based on replicate analysis of rhyolitic reference materials, is presented as a footnote in this table.

| Grain # | Grain Size (µm) | $SiO_2$ | $TiO_2$ | $Al_2O_3$ | FeOT | MnO | MgO | CaO | $Na_2O$ | $K_2O$ | $P_2O5$ |
|---|---|---|---|---|---|---|---|---|---|---|---|
| 1 | 40 | 71.52 | 1.37 | 14.87 | 2.38 | 0.02 | 0.27 | 1.26 | 4.87 | 3.3 | 0.14 |
| 2 | 20 | 73.64 | 0.94 | 14.9 | 1.99 | 0 | 0.24 | 1.26 | 3.59 | 3.33 | 0.09 |
| 3 | 30 | 72.6 | 0.62 | 15.04 | 2.31 | 0 | 0.27 | 1.22 | 4.5 | 3.27 | 0.17 |
| 4 | 50 | 71.64 | 1.27 | 14.97 | 2.16 | 0.02 | 0.32 | 1.22 | 5.1 | 3.29 | 0 |
| 5 | 40 | 72.58 | 1.01 | 14.89 | 1.68 | 0 | 0.3 | 0.91 | 5.46 | 2.97 | 0.2 |
| 6 | 45 | 72.37 | 0.82 | 14.93 | 2.31 | 0.02 | 0.25 | 1.23 | 4.78 | 3.1 | 0.19 |
| 7 | 20 | 73 | 1 | 15.02 | 2.08 | 0.01 | 0.23 | 1.18 | 4.2 | 3.28 | 0 |
| 8 | 20 | 72.76 | 1.12 | 14.92 | 2.07 | 0.01 | 0.3 | 1.24 | 4.18 | 3.32 | 0.1 |
| 10 | 20 | 71.4 | 1.45 | 14.65 | 2.37 | 0.02 | 0.32 | 1.25 | 5.06 | 3.36 | 0.11 |
| 11 | 80 | 71.77 | 1.06 | 14.89 | 2.24 | 0.02 | 0.29 | 1.17 | 5.56 | 3 | 0 |
| 12 | 20 | 71.77 | 1.25 | 14.84 | 2.34 | 0.02 | 0.28 | 1.33 | 4.8 | 3.37 | 0 |
| 13 | 15 | 70.96 | 1.56 | 14.84 | 2.46 | 0.03 | 0.3 | 1.17 | 5.35 | 3.09 | 0.25 |
| 14 | 15 | 71.47 | 1.61 | 14.48 | 2.61 | 0.02 | 0.17 | 1.34 | 4.43 | 3.61 | 0.28 |
| 15 | 20 | 72.75 | 1.19 | 14.59 | 2.02 | 0.01 | 0.31 | 1.3 | 4.38 | 3.33 | 0.13 |
| 16 | 50 | 71.58 | 1.41 | 15.07 | 2.26 | 0.02 | 0.37 | 1.29 | 4.56 | 3.32 | 0.12 |
| 17 | 20 | 72.26 | 0.93 | 14.85 | 2.18 | 0.01 | 0.27 | 1.21 | 4.96 | 3.32 | 0 |
| | **Avg.** | **72.13** | **1.16** | **14.86** | **2.22** | **0.01** | **0.28** | **1.22** | **4.74** | **3.27** | **0.11** |
| | **1 St. Dev.** | **0.72** | **0.28** | **0.16** | **0.22** | **0.01** | **0.05** | **0.1** | **0.52** | **0.16** | **0.09** |
| | **n =** | **16** | | | | | | | | | |

*Note: Analytical precision, based on replicate analyses of a rhyolitic reference material, is as follows (all in wt.%):*

*Rhyolite: $SiO_2$±1.40, $TiO_2$±0.71, $Al_2O_3$± 0.57, FeO±1.19, MnO±0.43, MgO± 0.09, CaO±0.53, $Na_2O$±1.39, $K_2O$±0.82, $P_2O_5$±0.11.*

**Table D.2.** GISP2 Glass Geochemistry (774.53-774.78 m depth), EPMA-WDS. All data were collected using EPMA-WDS at the University of Maine. All measurements are given in weight percent oxide and are normalized to 100% weight percent. "n" represents the total number of analyses. Analytical accuracy and precision are reported in Tables (D.3. and D.4.) and analytical methods are presented in Appendix C.5.

| Grain # | Point # | $SiO_2$ | $TiO_2$ | $Al_2O_3$ | FeOT | MnO | MgO | CaO | $Na_2O$ | $K_2O$ | $P_2O5$ | Cl | F | $SO_2$ |
|---|---|---|---|---|---|---|---|---|---|---|---|---|---|---|
| 1 | 1 | 71.80 | 0.53 | 15.09 | 2.12 | 0.15 | 0.48 | 1.70 | 4.69 | 3.04 | 0.10 | 0.19 | 0.11 | 0.01 |
| 1 | 3 | 73.75 | 0.51 | 15.68 | 2.00 | 0.15 | 0.49 | 1.57 | 2.38 | 3.10 | 0.08 | 0.18 | 0.10 | 0.01 |
| 2 | 1 | 71.15 | 0.52 | 15.58 | 2.25 | 0.16 | 0.48 | 1.61 | 4.96 | 2.93 | 0.09 | 0.21 | 0.04 | 0.01 |
| 3 | 3 | 71.91 | 0.53 | 14.70 | 2.33 | 0.16 | 0.48 | 1.74 | 4.76 | 2.97 | 0.09 | 0.19 | 0.13 | 0.01 |
| 6 | 1 | 70.78 | 0.54 | 15.40 | 2.36 | 0.16 | 0.49 | 1.68 | 4.90 | 3.34 | 0.09 | 0.20 | 0.06 | 0.01 |
| 6 | 2 | 71.94 | 0.54 | 15.12 | 2.24 | 0.16 | 0.46 | 1.71 | 4.34 | 3.19 | 0.08 | 0.20 | 0.04 | 0.00 |
| 6 | 3 | 72.86 | 0.54 | 14.20 | 2.46 | 0.15 | 0.56 | 1.61 | 4.14 | 3.26 | 0.09 | 0.20 | -0.07 | 0.01 |
| 7 | 1 | 71.41 | 0.50 | 15.45 | 2.36 | 0.15 | 0.52 | 1.82 | 4.84 | 3.10 | 0.09 | 0.21 | -0.47 | 0.01 |
| 7 | 2 | 70.26 | 0.53 | 16.19 | 2.19 | 0.16 | 0.55 | 1.83 | 4.96 | 3.21 | 0.10 | 0.23 | -0.21 | 0.00 |
| 8 | 1 | 71.41 | 0.53 | 15.51 | 2.26 | 0.16 | 0.50 | 1.64 | 4.39 | 3.14 | 0.13 | 0.26 | 0.06 | 0.01 |
| 9 | 1 | 71.90 | 0.54 | 15.22 | 2.16 | 0.16 | 0.45 | 1.67 | 4.52 | 3.10 | 0.10 | 0.20 | -0.03 | 0.01 |
| 10 | 1 | 70.30 | 0.51 | 16.17 | 2.46 | 0.16 | 0.47 | 1.59 | 4.87 | 3.10 | 0.12 | 0.26 | -0.01 | 0.01 |
| 10 | 2 | 69.78 | 0.51 | 15.77 | 2.46 | 0.16 | 0.53 | 1.75 | 5.28 | 3.13 | 0.14 | 0.31 | 0.17 | 0.01 |
| 10 | 3 | 71.03 | 0.47 | 15.68 | 2.37 | 0.15 | 0.51 | 1.71 | 4.44 | 3.13 | 0.13 | 0.33 | 0.05 | 0.01 |
| 10 | 4 | 69.92 | 0.51 | 15.46 | 2.65 | 0.16 | 0.54 | 1.71 | 5.26 | 3.17 | 0.17 | 0.43 | -0.04 | 0.06 |
| 10 | 5 | 70.58 | 0.54 | 15.06 | 2.16 | 0.16 | 0.53 | 1.77 | 5.38 | 3.33 | 0.12 | 0.24 | 0.12 | 0.01 |
| 11 | 1 | 71.17 | 0.49 | 15.09 | 2.38 | 0.16 | 0.50 | 1.68 | 4.75 | 3.06 | 0.19 | 0.29 | 0.18 | 0.05 |
| 13 | 1 | 73.24 | 0.53 | 14.01 | 2.16 | 0.15 | 0.49 | 1.70 | 4.44 | 3.03 | 0.10 | 0.21 | -0.07 | 0.01 |
| 14 | 1 | 71.96 | 0.53 | 15.24 | 2.35 | 0.15 | 0.54 | 1.68 | 4.17 | 3.12 | 0.10 | 0.20 | -0.03 | 0.01 |
| | **Avg.** | **71.43** | **0.52** | **15.29** | **2.30** | **0.16** | **0.50** | **1.69** | **4.60** | **3.13** | **0.11** | **0.24** | **0.01** | **0.01** |
| | **1 St. Dev.** | **1.08** | **0.02** | **0.56** | **0.15** | **0.01** | **0.03** | **0.07** | **0.65** | **0.11** | **0.03** | **0.06** | **0.15** | **0.02** |
| | **n =** | **19** | | | | | | | | | | | | |

*Note: Analytical precision, based on replicate analyses of a rhyolitic reference material, is as follows (all in wt.%):*

*Rhyolite: $SiO_2$±1.76, $TiO_2$±0.01, $Al_2O_3$± 2.22, FeO±0.15, MnO±0.00, MgO± 0.01, CaO±0.04, $Na_2O$±0.26, $K_2O$±0.18, $P_2O_5$±0.00, Cl±0.01, F±0.07, SO2±0.00.*

**Table D.3.** EPMA-WDS Measurements on Basaltic Glass Standard. "N" represents the total number of analyses.

| Basaltic Glass NMNH 113498-I (A99) | | | | | | | | | | | | | | |
|---|---|---|---|---|---|---|---|---|---|---|---|---|---|---|
| | $SiO_2$ | $TiO_2$ | $Al_2O_3$ | FeOT | MnO | MgO | CaO | $Na_2O$ | $K_2O$ | $P_2O5$ | Cl | F | $SO_2$ | N |
| Avg | 50.82 | 4.10 | 13.38 | 13.29 | 0.20 | 5.12 | 9.14 | 2.57 | 0.85 | 0.46 | 0.02 | 0.01 | 0.02 | 20 |
| st. dev. | 0.40 | 0.06 | 0.48 | 0.24 | 0.01 | 0.08 | 0.14 | 0.15 | 0.04 | 0.01 | 0.00 | 0.08 | 0.00 | 20 |
| **Accepted Value*** | | | | | | | | | | | | | | |
| | 50.94 | 4.06 | 12.49 | 13.3 | 0.15 | 5.08 | 9.30 | 2.66 | 0.82 | 0.38 | 0.13 | - | - | - |

*Accepted Value: Jarosewich, E., Nelen, J. A., and Norberg, J. A. (1980).

**Table D.4**. EPMA-WDS Measurements on Rhyolitic Glass Standard. "N" represents the total number of analyses.

| Rhyolitic Glass, NMNH 72854 | | | | | | | | | | | | | | |
|---|---|---|---|---|---|---|---|---|---|---|---|---|---|---|
| | $SiO_2$ | $TiO_2$ | $Al_2O_3$ | FeOT | MnO | MgO | CaO | $Na_2O$ | $K_2O$ | $P_2O5$ | Cl | F | $SO_2$ | N |
| Avg | 77.31 | 0.09 | 12.18 | 1.10 | 0.03 | 0.03 | 0.44 | 3.60 | 4.95 | 0.00 | 0.10 | 0.16 | 0.00 | 20 |
| st. dev. | 1.76 | 0.01 | 2.22 | 0.15 | 0.00 | 0.01 | 0.04 | 0.26 | 0.18 | 0.00 | 0.01 | 0.07 | 0.00 | 20 |
| **Accepted Value*** | | | | | | | | | | | | | | |
| | 76.71 | 0.12 | 12.06 | 1.28 | 0.03 | <0.10 | 0.50 | 3.75 | 4.89 | <0.01 | 0.13 | - | - | - |

*Accepted Value: Jarosewich, E., Nelen, J. A., and Norberg, J. A. (1980).

## BIOGRAPHY OF THE AUTHOR

Meredith Helmick, known by those close to her as “Mere” or “Mert”, was born and raised in Marion County, West Virginia. By the aid of her parents and several jeep trips to riverside camp sites, state parks, and Leadmine Run; she developed a strong connection with the natural world she often found herself exploring. This connection continued into her teen and young adult years, and she found herself kayaking, hiking, and rock climbing throughout central Appalachia. Through these activities, her connection to the natural world grew into a frenzied desire to learn how this natural world operated. After several years exploring and working in public service, Meredith resumed her education and earned a bachelor’s degree in Environmental Geoscience from Concord University.

While at Concord, Meredith was advised by Dr. Stephen Kuehn who introduced her to the world of tephra and microanalysis. She was also fortunate enough to make a lifelong friend out of professor, friend, and soon-to-be PhD, Jennifer Phillippe, who co-advised her through her first research proposal, expedition, and independent research project.

In summer 2020, Meredith made the insane decision to pursue an advanced degree at the University of Maine during a global pandemic. Meredith is a candidate for the Master of Science degree in Earth and Climate Science from the University of Maine in December 2022.